OPEN ACCESS Freely available online

PLoS one

Pairing Mechanism for the High-T_C Superconductivity: Symmetries and Thermodynamic Properties

Radosław Szczęśniak*

Institute of Physics, Częstochowa University of Technology, Częstochowa, Poland

Abstract

The pairing mechanism for the high-T_C superconductors based on the electron-phonon (EPH) and electron-electron-phonon (EEPH) interactions has been presented. On the *fold* mean-field level, it has been proven, that the obtained *s*-wave model supplements the predictions based on the BCS van Hove scenario. In particular: (i) For strong EEPH coupling and $T<T_C$ the energy gap (Δ_{tot}) is very weak temperature dependent; up to the critical temperature Δ_{tot} extends into the anomalous normal state to the Nernst temperature. (ii) The model explains well the experimental dependence of the ratio $R_1 \equiv 2\Delta_{tot}^{(0)}/k_B T_C$ on doping for the reported superconductors in the terms of the few fundamental parameters. In the presented paper, the properties of the *d*-wave superconducting state in the two-dimensional system have been also studied. The obtained results, like for *s*-wave, have shown the energy gap amplitude crossover from the BCS to non-BCS behavior, as the value of the EEPH potential increases. However, for $T>T_C$ the energy gap amplitude extends into the anomalous normal state to the pseudogap temperature. Finally, it has been presented that the anisotropic model explains the dependence of the ratio R_1 on doping for the considered superconductors.

Citation: Szczęśniak R (2012) Pairing Mechanism for the High-T_C Superconductivity: Symmetries and Thermodynamic Properties. PLoS ONE 7(4): e31873. doi:10.1371/journal.pone.0031873

Editor: Ruihua He, Lawrence Berkeley National Laboratory, United States of America

Received October 19, 2011; **Accepted** January 13, 2012; **Published** April 18, 2012

Funding: This work is supported by Czestochowa University of Technology, BS/PB-203-301/2011. The funders had no role in the study design, data collection and analysis, decision to publish, or preparation of the manuscript.

Competing Interests: The author has declared that no competing interests exist.

* E-mail: szczesni@wip.pcz.pl

Introduction

In the study, we present the microscopic theory of the high-T_C superconductivity [1], [2]. The organization of the paper is as follows:

In Section II (subsection 1) we call for the pairing mechanism. First of all, we discuss the main experimental and theoretical results. Next, on the basis of the presented analysis, we give the postulates, which determine the microscopic model for the high-T_C superconductors in the second quantization form.

In Section II (subsection 2), by using the unitary transformation, we deduce from the initial Hamiltonian the simple mean-field model. In the framework of the toy model (only the *s*-wave state), we discuss the properties of the energy gap in the superconducting and Nernst region; the numerical predictions are supplemented by the analytical approach. Next, for selected high-T_C superconductors, we calculate the fundamental parameters of the model and compare the obtained theoretical results with the experimental data.

In Section II (subsection 3) we study the theromodynamic properties of the *d*-wave superconducting state in the two-dimensional system. We test the anisotropic model for the considered high-T_C superconductors.

Finally, in Section III we summarize the results.

Results

The Pairing Mechanism

The real cuprates are three-dimensional. However, their physical properties are strongly anisotropic. On the basis of very small coherence length in the c direction (smaller than the interplane distance) one can suppose that the CuO_2 electrons play the special role in the physics of the high-T_C superconductors [3]. Unfortunately, the pairing mechanism for the planar problem remains highly controversial and many different hypotheses are suggested. In the literature two fundamental directions in search for the pairing mechanism have been crystallized. The first approach is based on the single-band Hubbard model, its extensions or related models *e.g.* $t-J$ model [4], [5], [6], [7], [8], [9], [10], [11], [12]; the second approach emphasizes the relevance of the electron-phonon interaction [13], [14], [15].

Why is the Hubbard model so much studied? First of all, some analysis suggest that the one-band Hubbard model reproduces well the spectra of the more complicated three-band Hamiltonian for electrons in the copper oxide planes (the Emery model) [3], [5], [6]. For example, by using the finite cluster method, Hybertsen *et al.* have shown that the one-band Hubbard model with the small next-nearest-neighbor integral t' should have the following parameters: $t=430$ meV, $t'=-70$ meV and $U_H=5.4$ eV [16]. Secondly, for the half-filled electron band and large on-site Coulomb interaction, the Hubbard model reduces to the Heisenbeg model, which describes well the spin dynamics of the underdoped high-T_C superconductors [3]. On the basis of the quoted facts some authors suppose, that the strong electronic correlations modeled by the Hubbard model can alone induce the superconducting state in the cuprates. Unfortunately, the studies carried out by several groups have shown that the Hubbard model gives no obvious evidence for superconductivity with the large critical temperature [17], [18], [19], [20]. On the

other hand, there is the strong tendency for superconductivity in the attractive Hubbard model for the same value of the on-site Coulomb interaction. Finally, we noticed that probably also the three-band Hubbard model and the $t-J$ model do not superconduct at temperatures characteristic for the cuprates [3], [21].

The relevance of phonons to the pairing mechanism in the high-T_C superconductivity also constitutes a complicated problem. On the one hand there exist many experimental observations which have been taken as evidence for the electron-phonon interaction in the cuprates. For example: the strong isotope effects on T_C in the underdoped superconductors [22], the phonon renormalization in the Raman measurements [23], the phonon-related features of $I-V$ characteristics obtained by using the tunnelling experiments [24], [25], [26] and the dependence of the penetration depth on the substitution O^{16} by O^{18} [27], [28]. Especially important results come from the ARPES measurements which give the evidence on the low-energy kink in the quasiparticle spectrum around the phonon energy both for the nodal and antinodal points [29], [30]; also the ARPES isotope effect in $\mathrm{Re}(\Sigma)$ has been observed [31]. On the other hand the first principles calculations support the view that the conventional electron-phonon coupling is small [32]. For example, Bohnen *et al.* have predicted that the electron-phonon coupling constant for $YBa_2Cu_3O_{7-y}$ is equal to 0.27; so the strong Hubbard correlations should completely suppress the phonon-mediated superconductivity [33].

After summarizing the mentioned experimental and theoretical results, one can conclude that: (i) the cuprates belong to the strongly correlated systems but probably these correlations in the superconductivity domain are beyond the Hubbard or related approaches, since in these models the pairing correlations are too small, (ii) in the cuprates the conventional electron-phonon interaction is small but according to the experimental data one can suppose that the phonons play the important role in the pairing mechanism.

In order to solve the problem of high temperature superconductivity we present and examine the following scenario:

•(i) In the superconductivity domain of the cuprates the fundamental role is played by the electrons on the CuO_2 planes.

•(ii) In the cuprates exists the conventional electron-phonon interaction, which has not to be strong.

•(iii) In the cuprates exist strong electronic correlations, but the electron-electron scattering in the superconductivity domain is inseparably connected with the absorption or emission of vibrational quanta.

In the simplest case the first and second postulate coincides with the phonon-van-Hove-scenario for high-T_C superconductors [34], [35]. The third postulate states that the effective electronic correlations in the superconductivity domain are connected with the three-body process: the electron-electron-phonon interaction. In Fig. 1 we show in detail the diagrammatic representation of this interaction. We notice that the EEPH coupling has a significant property which distinguish it from the Hubbard interaction; it does not destroy the classical phonon-mediated pairing correlations. Additionally, one should pay attention to the fact, that the first postulate has also the essential significance for the third postulate. Namely, for the two-dimensional case (the van Hove singularity at the Fermi level), the EEPH coupling has significantly strong influence on the physical properties of the system (see next subsection).

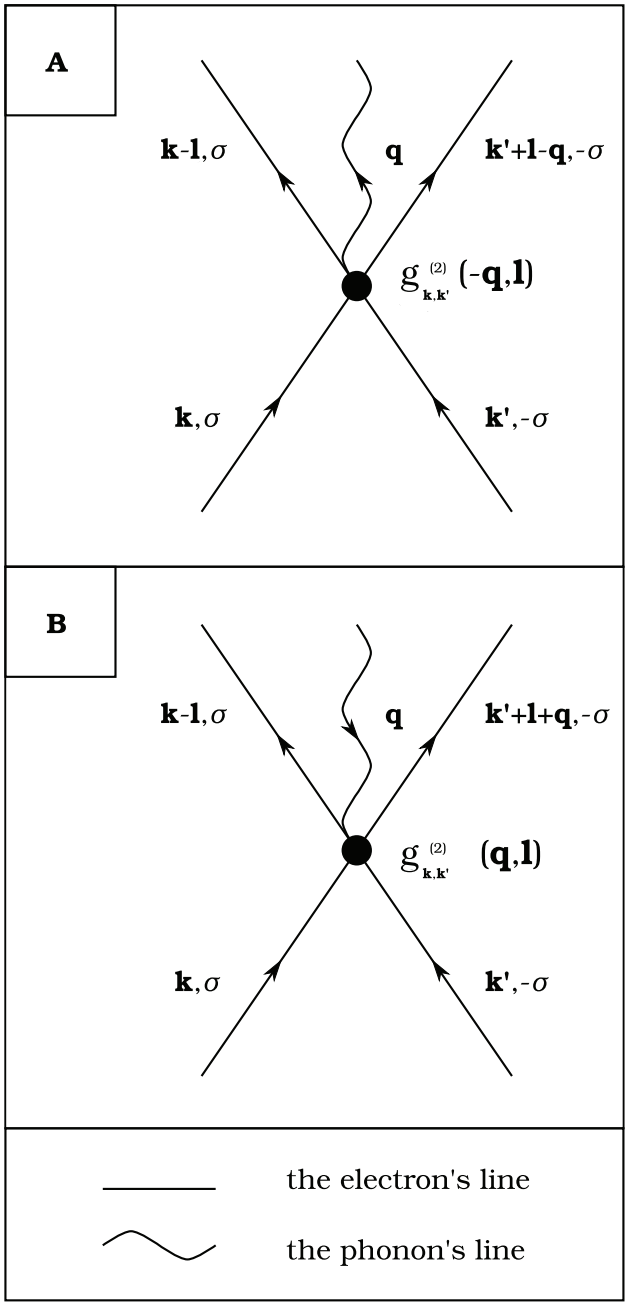

Figure 1. The graphical representation of the electron-electron-phonon coupling. The electron states are represented by the straight lines, while the phonon state by the curly line. The vertex is denoted by the black dot and its strength is given by $g^{(2)}_{k,\,k'}(q,l)$. In Fig. 1 (A) the electrons emit the phonon during the scattering; in Fig. 1 (B) the electrons absorb the phonon.
doi:10.1371/journal.pone.0031873.g001

Below, we consider the Hamiltonian that describes the postulated coupling of the correlated electrons to phonons in the second quantization form:

$$H \equiv H^{(0)} + H^{(1)} + H^{(2)}. \tag{1}$$

The first term represents the non-interacting electrons and phonons:

$$H^{(0)} \equiv \sum_{\mathbf{k}\sigma} \overline{\varepsilon_{\mathbf{k}}} c^{\dagger}_{\mathbf{k}\sigma} c_{\mathbf{k}\sigma} + \sum_{\mathbf{q}} \omega_{\mathbf{q}} b^{\dagger}_{\mathbf{q}} b_{\mathbf{q}}, \tag{2}$$

where $\overline{\varepsilon_{\mathbf{k}}} \equiv \varepsilon_{\mathbf{k}} - \mu$; $\varepsilon_{\mathbf{k}}$ and μ denotes the electron band energy and the chemical potential respectively. For the two-dimensional square lattice and the nearest-neighbor hopping integral t, we have: $\varepsilon_{\mathbf{k}} = -t\gamma(\mathbf{k})$, where $\gamma(\mathbf{k}) \equiv 2\left[\cos(k_x) + \cos(k_y)\right]$. The symbol $\omega_{\mathbf{q}}$ stands for the energy of phonons. The interaction terms are given by:

$$H^{(1)} \equiv \sum_{\mathbf{kq}\sigma} g^{(1)}_{\mathbf{k}}(\mathbf{q}) c^{\dagger}_{\mathbf{k}} + \mathbf{q}\sigma \mathbf{c}_{\mathbf{k}\sigma}\phi_{\mathbf{q}}, \tag{3}$$

and

$$H^{(2)} \equiv \sum_{\mathbf{kk'ql}\sigma} g^{(2)}_{\mathbf{k},\mathbf{k'}}(\mathbf{q},\mathbf{l}) c^{\dagger}_{\mathbf{k}-\mathbf{l}\sigma} c_{\mathbf{k}\sigma} c^{\dagger}_{\mathbf{k'}+\mathbf{l}+\mathbf{q}-\sigma} c_{\mathbf{k'}-\sigma}\phi_{\mathbf{q}}, \tag{4}$$

where $\phi_{\mathbf{q}} \equiv b^{\dagger}_{-\mathbf{q}} + b_{\mathbf{q}}$. The matrix elements $g^{(1)}_{\mathbf{k}}(\mathbf{q})$ describe the electron-phonon interaction [36], [37] and the symbol $g^{(2)}_{\mathbf{k},\mathbf{k}}(\mathbf{q},\mathbf{l})$ determines the strength of the electron-electron-phonon coupling. Since the Hamiltonian is the hermitian operator, we have: $g^{\star(1)}_{\mathbf{k}}(\mathbf{q}) = g^{(1)}_{\mathbf{k}+\mathbf{q}}(-\mathbf{q})$ and $g^{\star(2)}_{\mathbf{k},\mathbf{k'}}(\mathbf{q},\mathbf{l}) = g^{(2)}_{\mathbf{k'}+\mathbf{l}+\mathbf{q},\mathbf{k}-\mathbf{l}}(-\mathbf{q},\mathbf{l}+\mathbf{q})$.

The Fold Mean-field Theory

From the mathematical point of view, the Hamiltonian (1) belongs to the class of so-called *dynamic Hubbard models*. These Hamiltonians describe modulation of the Hubbard on-site repulsion by the boson degree of freedom and were studied in detail by J.E. Hirch, F. Marsiglio and R. Teshima in the papers [38], [39], [40].

In the simplest case ($U_H = 0$), the dynamic Hubbard Hamiltonian describes the Holstein-like electron-boson interaction, where the coupling constant increases with the electron occupation. This model, however interesting, is inappropriate in the description of the high-T_C superconductivity. In the more elaborate scheme, the properties of the dynamic Hubbard model, can be studied by using the generalized Lang-Firsov transformation: $H' = e^{S} H e^{-S}$, where the generator S has the form:

$S \equiv \sum_j g\left(b_j - b_j^{\dagger}\right)\left(n_{j\uparrow} + n_{j\downarrow} - n_{j\uparrow} n_{j\downarrow}\right)$ and $n_{j\sigma}$ is the number operator for the site j and the spin σ. Next, the obtained effective Hamiltonian should be analyzed in the framework of the Eliashberg-like approximation [40], [41], [42], [43], [44], [45]; the central result is that the critical temperature increases with retardation.

We notice that the form of the Hamiltonan (1) suggests using the Eliashberg approach in order to analyse the physical properties of the considered system [42], [43], [44], [45]. This method is appropriate, because one can retain simultaneously the electron and phonon degrees of freedom. The detailed calculations in the framework of the Eliashberg approach the reader can to trace in: [46], [47], [48], [49], [50], [51], [52], [53], [54], [55]. Additionally, in the framework of the Eliashberg formalism, the formally exact expression for the self-energy matrix is easy to determine. The analysis of the above issue is presented in Appendix S1, where we have shown that: (i) in the case of the absence of the lattice distortion, the first-order contribution to the self-energy is equal to zero, (ii) the electron-phonon coupling is directly increased by the electron-electron-phonon interaction, (iii) the form of the second-order contributions to the matrix self-energy is very complicated. Unfortunately, this fact hampers considerably the detailed calculations on the Eliashberg level.

In the case of the presented paper, we have eliminated the phonon operators only from the EEFH term. The obtained Hamiltonian is next added to the BCS operator [56], [57]. As discussed in the following subsubsections, presented approximate description represents a generalization of the BCS van Hove scenario [35].

The unitary transformation. In order to eliminate the phonon degrees of freedom in the Hamiltonian (4) we use the Fröhlich-type unitary transformation:

$$H' \equiv e^{-iS}\left(H^{(0)} + H^{(2)}\right)e^{iS}, \tag{5}$$

where the operator S denotes the generator:

$$S \equiv \sum_{\mathbf{q}} S_{\mathbf{q}}. \tag{6}$$

In our case: $S_{\mathbf{q}} \equiv \gamma_{\mathbf{q}} b_{\mathbf{q}} + \gamma^{\dagger}_{\mathbf{q}} b^{\dagger}_{\mathbf{q}}$, where.

$$\gamma_{\mathbf{q}} \equiv \sum_{\mathbf{kl}\sigma} \Phi(\mathbf{k},\mathbf{k'},\mathbf{l},\mathbf{q}) c^{\dagger}_{\mathbf{k}-\mathbf{l}\sigma} c_{\mathbf{k}\sigma} c^{\dagger}_{\mathbf{k'}+\mathbf{l}+\mathbf{q}-\sigma} c_{\mathbf{k'}-\sigma}. \tag{7}$$

The expression (5) can be rewritten in the approximate form:

$$\begin{aligned} H' \simeq H^{(0)} + \left(i[H^{(0)},S]_{-} + H^{(2)}\right) \\ + i\left[\left(\frac{i}{2}\left[H^{(0)},S\right]_{-} + H^{(2)}\right),S\right]_{-}, \end{aligned} \tag{8}$$

where the square brackets $[,]_{-}$ denote the commutator. To eliminate the second term in Eq. (8) we assume that the generator fulfills the relation: $i[H^{(0)},S]_{-} + H^{(2)} = 0$, hence:

$$\Phi(\mathbf{k},\mathbf{k'},\mathbf{l},\mathbf{q}) = \frac{i g^{(2)}_{\mathbf{k},\mathbf{k'}}(\mathbf{q},\mathbf{l})}{\varepsilon_{\mathbf{k}-\mathbf{l}} - \varepsilon_{\mathbf{k}} + \varepsilon_{\mathbf{k'}+\mathbf{l}+\mathbf{q}} - \varepsilon_{\mathbf{k'}} - \omega_{\mathbf{q}}}. \tag{9}$$

Next, we can reduce the Hamiltonian H' to the following expression:

$$\begin{aligned} H_{eff} \equiv <0_{\mathrm{ph}}|H'|0_{\mathrm{ph}}> \simeq \sum_{\mathbf{k}\sigma} \overline{\varepsilon_{\mathbf{k}}} c^{\dagger}_{\mathbf{k}\sigma} c_{\mathbf{k}\sigma} + \sum_{\mathbf{kk'ql}\sigma} U_{\mathbf{k},\mathbf{k'}} \\ (\mathrm{q},\mathrm{l}) c^{\dagger}_{\mathbf{k}-\mathrm{l}\sigma} c_{\mathbf{k}\sigma} c^{\dagger}_{\mathbf{k'}+\mathrm{l}+\mathrm{q}-\sigma} \\ c_{\mathbf{k'}-\sigma} c^{\dagger}_{-\mathbf{k'}-\mathrm{l}-\mathrm{q}\sigma} c_{-\mathbf{k'}\sigma} c^{\dagger}_{-\mathbf{k}+\mathrm{l}-\sigma} c_{-\mathbf{k}-\sigma}, \end{aligned} \tag{10}$$

where the phonon vacuum state is given by $|O_{\mathrm{ph}}>$. The pairing potential $U_{\mathbf{k},\mathbf{k'}}(\mathbf{q},\mathbf{l})$ is of the form:

$$U_{\mathbf{k},\mathbf{k'}}(\mathbf{q},\mathbf{l}) \simeq \frac{\omega_0 |g^{(2)}|^2}{\left(\varepsilon_{\mathbf{k}} - \varepsilon_{\mathbf{k}-\mathbf{l}} + \varepsilon_{\mathbf{k'}} - \varepsilon_{\mathbf{k'}+\mathbf{l}+\mathbf{q}}\right)^2 - \omega_0^2}. \tag{11}$$

We assume additionally that: $g^{(2)}_{\mathbf{k},\mathbf{k'}}(\mathbf{q},\mathbf{l}) \simeq g^{(2)}$ and $\omega_{\mathbf{q}} \simeq \omega_0$; the symbol ω_0 denotes the characteristic phonon frequency. On the

basis of the expression (10) we conclude that the EEPH interaction can be replaced by the effective four electron-electron (4EE) scattering event; the diagrammatic representation of this interaction is shown in Fig. 2. From the Eq. (11) it is clear that the effective potential is attractive if: $|\varepsilon_{\mathbf{k}}-\varepsilon_{\mathbf{k}-\mathbf{l}}+\varepsilon_{\mathbf{k}'}-\varepsilon_{\mathbf{k}'+\mathbf{l}+\mathbf{q}}|<\omega_0$. In the subsection, we consider the simplest case, when the attractive part of the 4EE potential can be written as:

$$U^{(<)}_{\mathbf{k},\mathbf{k}'}(\mathbf{q},\mathbf{l})\rightarrow -\frac{U}{24N^3}, \tag{12}$$

for $|\varepsilon_{\mathbf{k}}|<\omega_0$. We have used the factor $\frac{1}{24}$, because the potential energy term represents the interaction between every four of particles counted once.

By using the *fold* mean-field (MF) approximation the Hamiltonian (10) takes the form (see also Appendix S2):

$$\begin{aligned} H^{MF}_{eff} &= \sum_{\mathbf{k}\sigma}\bar{\varepsilon}_{\mathbf{k}}\,c^{\dagger}_{\mathbf{k}\sigma}c_{\mathbf{k}\sigma} \\ &- \frac{U}{12}\sum_{\mathbf{k}\sigma}^{\omega_0}|\Delta_{\sigma}|^2\left(\Delta_{\sigma}c^{\dagger}_{\mathbf{k}-\sigma}c^{\dagger}_{-\mathbf{k}\sigma}+\Delta^{\star}_{\sigma}c_{-\mathbf{k}\sigma}c_{\mathbf{k}-\sigma}\right). \end{aligned} \tag{13}$$

The symbol $\sum_{\mathbf{k}}^{\omega_0}$ denotes the sum over the states when the 4EE potential is attractive;

$$\Delta_{\sigma}\equiv\frac{1}{N}\sum\nolimits_{\mathbf{k}}^{\omega_0}<c_{-\mathbf{k}\sigma}c_{\mathbf{k}-\sigma}>$$

The toy model. The thermodynamic parameters of the high-T_C superconductors can have essentially different properties in comparison with the low-T_C materials. From this reason, the analysis of the results obtained in the framework of the simplest approach is important, because these predictions facilitate the interpretation of the fundamental experimental data.

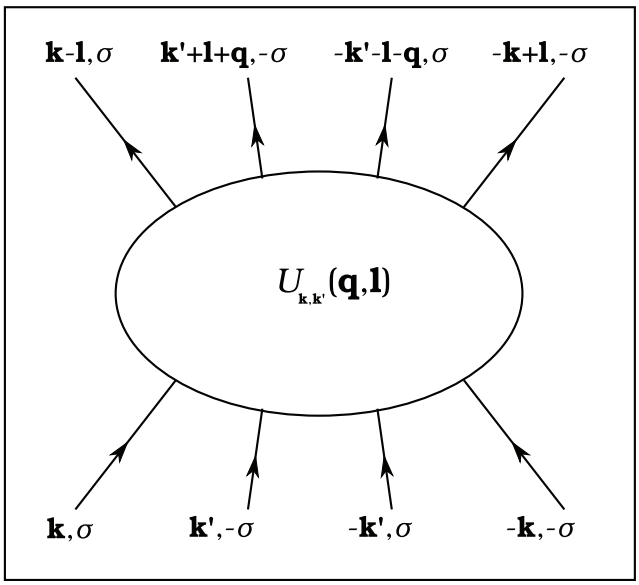

Figure 2. The four-body scattering event contributing to the interaction part of the Hamiltonian (10). The oval connecting the electron's lines is an illustration of $U_{\mathbf{k},\mathbf{k}'}(\mathbf{q},\mathbf{l})$ which denotes the effective potential.
doi:10.1371/journal.pone.0031873.g002

Taking into account the operator (13) we can write the total Hamiltonian in the form:

$$\begin{aligned} H^{MF} &\equiv \sum_{\mathbf{k}\sigma}\varepsilon_{\mathbf{k}}c^{\dagger}_{\mathbf{k}\sigma}c_{\mathbf{k}\sigma} \\ &-\left(V+\frac{U}{6}|\Delta|^2\right)\sum_{\mathbf{k}}^{\omega_0}\left(\Delta c^{\dagger}_{\mathbf{k}\uparrow}c^{\dagger}_{-\mathbf{k}\downarrow}+\Delta^{\star}c_{-\mathbf{k}\downarrow}c_{\mathbf{k}\uparrow}\right), \end{aligned} \tag{14}$$

where we have omitted the chemical potential and $\Delta\equiv\Delta_{\downarrow}$. In Eq. (14), the symbol V represents the BCS pairing potential obtained from the Hamiltonian (3).

Now, we establish the energy scales in the presented model. The nearest-neighbor hopping integral t is of the order of (200–400) meV [58], [59], [60], [61]. We notice that in the numerical model calculations we take t as an energy unit. From the *ab initio* calculations arises the fact that $V\in(0,2t)$ [33]. In order to determine qualitatively the possible values of U, we note, that the simple BCS pairing potential is obtained from the expression:

$$\frac{\omega_0|g^{(1)}|^2}{\left(\varepsilon_{\mathbf{k}}-\varepsilon_{\mathbf{k}+\mathbf{q}}\right)^2-\omega_0^2}\rightarrow-\frac{V}{2N}, \tag{15}$$

where the characteristic phonon frequency ω_0 is of the order of Debye frequency ($\omega_D\sim0.3t$); the electron-phonon coefficient $g^{(1)}$ has nearly the same value [62]. Next, we assume that the largest energy in the high-T_C superconductors, of order (5–10) eV, is the electron-electron-phonon potential; in the other words $g^{(2)}$ is comparable with the Coulomb repulsion in the one-band Hubbard model. Hence, $g^{(2)}/g^{(1)}\sim10^2$. Then, by using Eqs. (11), (12) and (15) we can calculate the ratio U/V. The result shows that U/V is proportional to $10\left(g^{(2)}/g^{(1)}\right)^2$. Due to this reason U/V can be considerably larger than $g^{(2)}/g^{(1)}$.

From the mathematical point of view, the value of U is not as much important as the value of the mean-field potential ($U_{MF}\equiv\frac{U}{6}|\Delta|^2$). It is easy to see that, in contrast to the BCS pairing potential, U_{MF} is Δ-dependent (the fundamental feature of the presented model). So, the potential U_{MF} depends on the temperature, V and U. If we set V and U the mean-field potential reaches the maximum value for $T=0$ K: $U^{(0)}_{MF}\equiv[U_{MF}]_{T=0}=\frac{U}{6}|\Delta^{(0)}|^2$, where the symbol $|\Delta^{(0)}|$ denotes the amplitude of the anomalous thermal average for $T=0$ K. In the case of the analyzed superconductors, we have $\left[U^{(0)}_{MF}\right]_{\max}\simeq3t$ (see also next subsubsection).

By using the Hamiltonian (14) we calculate the anomalous Green function:

$$<<c_{\mathbf{k}\uparrow}|c_{-\mathbf{k}\downarrow}>>=-\frac{\left(V+\frac{U}{6}|\Delta|^2\right)\Delta}{\omega^2-E^2_{\mathbf{k}}}, \tag{16}$$

where $E_{\mathbf{k}}\equiv\sqrt{\varepsilon^2_{\mathbf{k}}+\left(V+\frac{U}{6}|\Delta|^2\right)^2|\Delta|^2}$. The obtained propagator is more complicated than the BCS Green function; peculiarly, we draw the readers' attention to the very intricate structure of the energy gap. Additionally, we notice that all omitted terms in anomalous Green function (in particular the terms linear with reference to Δ in the pairing potential) are unimportant since they are at most of $\frac{1}{N}$ order (see Appendix S3). The fundamental equation can be found in the form:

$$1=\left(V+\frac{U}{6}|\Delta|^2\right)\frac{1}{N}\sum_{\mathbf{k}}^{\omega_0}\frac{1}{2E_{\mathbf{k}}}\tanh\frac{\beta E_{\mathbf{k}}}{2}. \quad (17)$$

In order to calculate the thermodynamic properties we transform the momentum summation over an energy integration in Eq. (17). We notice that, in the case of three-dimensional system, where the electron density of states near the Fermi energy is constant, the mean-field 4EE interaction can be neglected because the value of $U_{MF}^{(0)}$ is very small. The situation changes dramatically for the two-dimensional system, where $U_{MF}^{(0)}$ can be even greater than V. Then:

$$1=V_{tot}\int_0^{\omega_0}d\varepsilon\rho(\varepsilon)\frac{\tanh\left(\frac{\beta}{2}E\right)}{E}, \quad (18)$$

where: $E\equiv\sqrt{\varepsilon^2+\Delta_{tot}^2}$, $\Delta_{tot}\equiv V_{tot}|\Delta|$ and $V_{tot}\equiv V+\frac{U}{6}|\Delta|^2$. In the case of the square lattice the density of states is given by [63], [64], [65], [66], [67], [68], [69], [70], [71], [72], [73]:

$$\rho(\varepsilon)=b_1\ln|\frac{\varepsilon}{b_2}|, \quad (19)$$

where $b_1=-0.04687t^{-1}$ and $b_2=21.17796t$.

In Figs. 3 and 4 we show the numerical solutions of Eq. (18) for increasing values of $U_{MF}^{(0)}$. Analysis of the presented results allows one to state that only for $U_{MF}^{(0)}\le U_C^{(0)}$ (where $U_C^{(0)}$ is some characteristic value) the gap equation has one solution. Above $U_C^{(0)}$ at T_C open the two new branches of the energy gap.

We notice that in the framework of the obtained mean-field model the 4EE interaction does not influence on the value of T_C; so, the critical temperature can be calculated by using the expression [63], [64]:

$$k_BT_C=ab_2e^{-\frac{1}{\lambda_1}}, \quad (20)$$

where

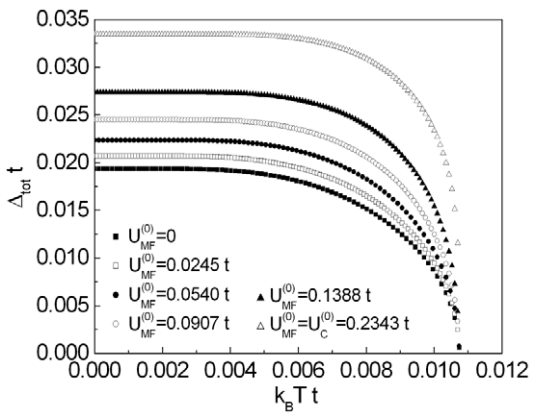

Figure 3. The dependence of Δ_{tot} on the temperature for $U_{MF}^{(0)}\le U_C^{(0)}=0.2343t$. We assume $V=1t$ and $\omega_0=0.3t$.
doi:10.1371/journal.pone.0031873.g003

$$\frac{1}{\lambda_1}\equiv\left[\ln^2(2a)+\ln^2\left(\frac{\omega_0}{b_2}\right)-\frac{2}{Vb_1}-2\right]^{\frac{1}{2}}, \quad (21)$$

and $a\equiv 2e^{\gamma}/\pi\simeq 1.13$ (γ is the Euler constant). In this case the isotope coefficient is small and can be calculated from: $\alpha=\frac{\lambda_1}{2}\ln\left(\frac{\omega_0}{b_2}\right)$.

Returning to the central line of the thought, it can be easily seen, that for both regions of $U_{MF}^{(0)}$ the values of Δ_{tot} strongly increase when $U_{MF}^{(0)}$ increases. For $U_{MF}^{(0)}>U_C^{(0)}$ the evolution of the gap parameter with the temperature is sharply different from the classical BCS prediction (see Fig. 4). In particular for $0<T<T_C$, the superconducting gap is very weak temperature dependent; this anomalous behavior is frequently observed in the cuprates [74], [75] The another important results are presented for $T_C<T<T^{**}$, where T^{**} denotes the highest value of the temperature for which the non-zero solution of the gap equation exists. In this case we have two branches. In order to find out, for which of these solutions the thermodynamic potential is lower, the numerical calculations have been made. The detailed analysis of this complicated issue is presented in the Appendix S4 (see also Fig. S1). As an example, in Fig. 5 we show the dependence of the difference of the thermodynamic potential between the non-zero gap state and the normal state ($\Delta\Omega_{VU}$) on the temperature. The obtained result proves, that the physical solution represents the higher branch; whereas the lower branch corresponds to the unstable state.

Next, the temperature T^{**} should be interpreted on the experimental background.

First, we notice that the complicated mathematical structure of the order parameter (in general, it is the complex function) imposes two conditions on the existence of the superconducting state: (i) the amplitude of the order parameter has to differ from zero and (ii) the superconducting state has to exhibit the long-range phase coherence.

The essential pointer, how should be interpreted the temperature T^{**}, is connected with the experiments based on the Nernst effect [8], [76]. Namely, the Nernst signal above T_C strongly suggests that the superconductivity vanishes at T_C because the long-range phase coherence is destroyed by the thermally created vortices. Additionally, the experimental data have shown that the amplitude of the order parameter extends into the "normal" state to the temperature T_{NE} (the Nernst temperature). We notice that T_{NE} is considerably much lower than the pseudogap temperature (T^*). On the basis of presented experimental facts and the obtained theoretical results we assume that $T^{**}=T_{NE}$.

Before the comparison between the experimental data and the theoretical results obtained in the framework of toy model, we supplement the analytical approach. First, we notice that for $T=0$ the integral equation (18) reduces to the algebraic equation:

$$\Delta_{tot}^{(0)}=2\omega_0e^{-\frac{1}{\lambda_2}}, \quad (22)$$

where the symbol $\Delta_{tot}^{(0)}$ denotes the gap parameter at zero temperature and

$$\frac{1}{\lambda_2}\equiv\ln\left(\frac{\omega_0}{b_2}\right)+\left[\ln^2\left(\frac{\omega_0}{b_2}\right)-\frac{2}{V_{tot}b_1}-\frac{\pi^2}{6}\right]^{\frac{1}{2}}. \quad (23)$$

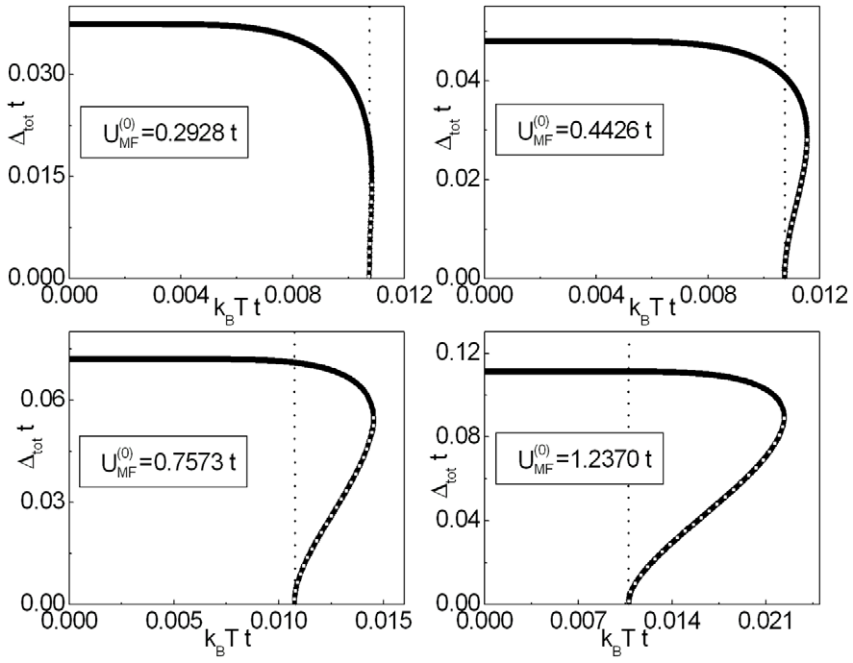

Figure 4. The dependence of Δ_{tot} on the temperature for $U_{MF}^{(0)} > U_C^{(0)}$. We assume $V = 1t$ and $\omega_0 = 0.3t$. The vertical line indicates a position of the critical temperature. For $T > T_C$ the solid line represents the higher branch, whereas the perforated line corresponds to the lower branch.
doi:10.1371/journal.pone.0031873.g004

By using the equation (22) and expression (20) one can easily calculate the ratio: $R_1 \equiv \dfrac{2\Delta_{tot}^{(0)}}{k_B T_C}$. In the classical BCS theory R_1 is the universal constant of the model and $[R_1]_{BCS} = 3.53$. In the case of the BCS van Hove scenario R_1 depends on the model parameters, however slightly ($[R_1]_{\max} \sim 4$). The results obtained in the framework of the toy model are shown in Fig. 6. We see that R_1 is always bigger than in the BCS van Hove scenario and for sufficiently big values of $U_{MF}^{(0)}$ the ratio R_1 achieves the physically acceptable values.

Next, we consider the low-value behavior of the energy gap ($\Delta_{tot}/k_B T_C << 1$). In this case, the equation (18) should be rewritten in the form:

$$1 = \frac{2V_{tot}}{\beta} \sum_{m=-\infty}^{+\infty} \int_0^{\omega_0} d\varepsilon \rho(\varepsilon) \frac{1}{\omega_m^2 + \varepsilon^2 + \Delta_{tot}^2}. \qquad (24)$$

The kernel of the Eq. (24) may be expanded in powers of Δ_{tot}:

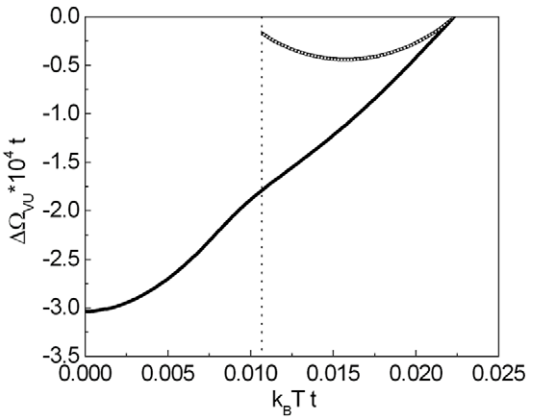

Figure 5. The dependence of $\Delta\Omega_{VU}$ on the temperature for $U_{MF}^{(0)} = 1.2370t$. We assume $V = 1t$ and $\omega_0 = 0.3t$. The vertical line indicates the position of the critical temperature. The solid line for $0 < T < T_C$ represents the result for the superconducting solution; the solid line for $T_C < T < T^{**}$ corresponds to the higher branch. The perforated line represents the thermodynamic potential for the lower branch. We notice that $\Delta\Omega_{VU}$ for the lower branch has the jump at T_C. This behavior is connected with the inversion of the solutions of Eq. (18) in the considered region viz., for V_1 and U_1 higher than V_2 and U_2 we have $\Delta_{tot}(V_1, U_1) < \Delta_{tot}(V_2, U_2)$.
doi:10.1371/journal.pone.0031873.g005

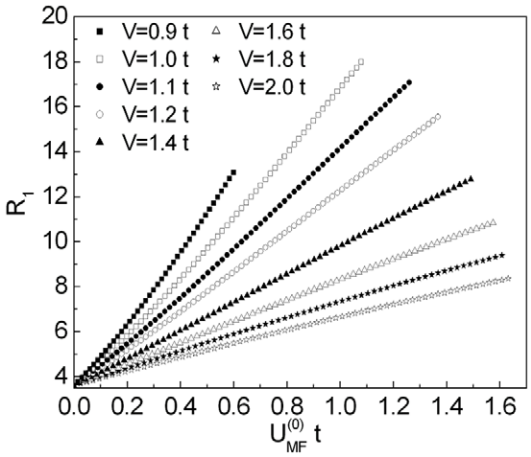

Figure 6. The dependence of the ratio R_1 on $U_{MF}^{(0)}$ for different values of V. We assume $\omega_0 = 0.3t$. We notice that the ratio R_1 is plotted for different maximal values of $U_{MF}^{(0)}$, since this quantity is also strong dependent on V.
doi:10.1371/journal.pone.0031873.g006

$$\frac{1}{\omega_m^2+\varepsilon^2+\Delta_{tot}^2} \simeq \frac{1}{\omega_m^2+\varepsilon^2} - \frac{\Delta_{tot}^2}{\left(\omega_m^2+\varepsilon^2\right)^2}. \quad (25)$$

Next, we assume $\omega_0 \to +\infty$, since $\omega_0 >> k_B T_C$. By using the lengthy but straightforward calculation we can transform the right-hand side of Eq. (24) into the algebraic form:

$$1 = b_1 V_{tot}\left[p_1(T) - p_2(T)\Delta_{tot}^2\right], \quad (26)$$

where

$$p_1(T) \equiv \ln\left(\frac{2k_BT}{b_2}\right)\ln\left(\frac{a\omega_0}{k_BT}\right) + \frac{1}{2}\ln^2\left(\frac{\omega_0}{2k_BT}\right) - 1, \quad (27)$$

and

$$p_2(T) \equiv \left(\frac{1}{\pi k_BT}\right)^2\left[\frac{7\zeta(3)}{8}\ln\left(\frac{\pi k_BT}{b_2 e}\right) + \vartheta(3)\right]. \quad (28)$$

The symbol ζ denotes the Riemann zeta function, ϑ is defined by: $\vartheta(z) \equiv \sum_{j=1}^{+\infty}(2j+1)^{-z}\ln(2j+1)$. If we omit the terms higher as $|\Delta|^4$ in Eq. (26), the expression for the anomalous thermal average takes the form:

$$|\Delta^{(\pm)}| \simeq \sqrt{\left[r_1(T) \pm \sqrt{r_1^2(T) + r_2(T)r_3(T)}\right]r_2^{-1}(T)}, \quad (29)$$

where:

$$r_1(T) \equiv \frac{1}{6}Up_1(T) - V^3p_2(T), \quad (30)$$

$$r_2(T) \equiv \frac{2}{3}UV^2p_2(T), \quad (31)$$

and

$$r_3(T) \equiv 2\left[p_1(T)V - \frac{1}{b_1}\right]. \quad (32)$$

We would like to point out that the expression (29) can be used only in the framework of the generalized mean-field model where $U \neq 0$; in the case of the BCS van Hove scenario the formula (29) generates the indeterminate form.

In Fig. 7 we illustrate the temperature dependence of the gap parameter close to T_C for different values of $U_{MF}^{(0)}$. In particular, we have shown the results obtained by using Eqs. (18) and (29); for comparison we calculate also the gap parameter in the BCS van Hove scenario. One can see that the approximate formula (29) very well reconstructs the exact numerical results both for the small and large values of $U_{MF}^{(0)}$; we strongly notice that for $U_{MF}^{(0)} > U_C^{(0)}$ exists only the unstable state.

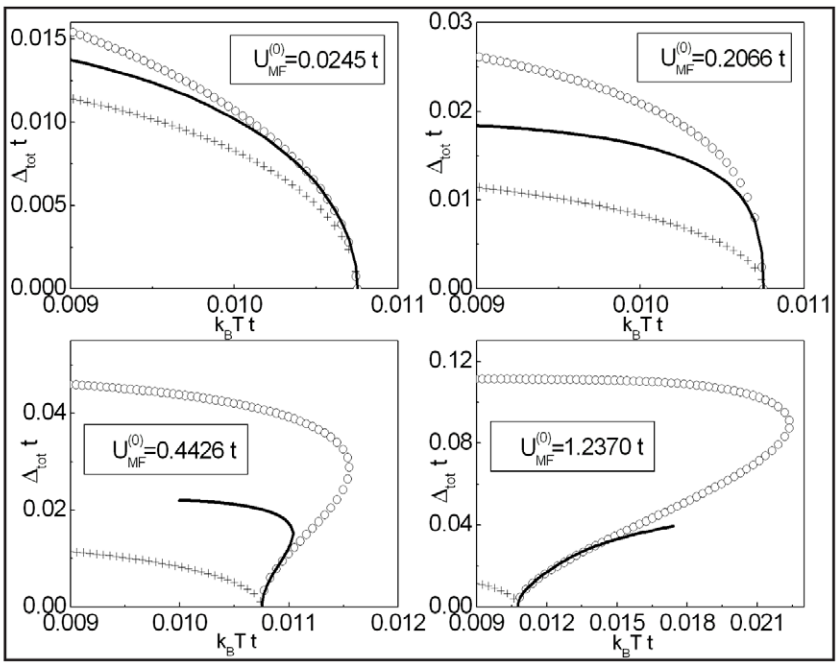

Figure 7. The dependence of Δ_{tot} on the temperature close to the transition temperature for the small and large values of $U_{MF}^{(0)}$. We assume $V = 1t$ and $\omega_0 = 0.3t$. The empty circles correspond to the exact numerical calculations (Eq. (18)). The solid line represents the calculation of Δ_{tot} by using the formula (29). The crosses are obtained in the BCS van Hove scenario.
doi:10.1371/journal.pone.0031873.g007

The toy model and the experimental results. The knowledge of the experimental values of T_C, T^{**} and other parameters (t and ω_0) enables the calculation of V and $U_{MF}^{(0)}$ for the real materials. In particular, the value of V is obtained by using the expression (20). Next, the potential $U_{MF}^{(0)}$ is determined from Eq. (18). We notice that, in principle, the quantities V and $U_{MF}^{(0)}$ can be determined for the underdoped, optimally doped or overdoped samples; one can even take under consideration the influence of the disorder on V and $U_{MF}^{(0)}$. This is possible, since the strength of the presented approach lies in fact that the physical state of the high-T_C materials in the superconductivity domain is well reproduced by the values of T_C and T^{**}. In general, the doping dependence can be calculated in the framework of the Eliashberg formalism. The initial study of this complicated issue has been presented in the paper [66].

In the subsubsection (for selected superconductors), on the basis of V and $U_{MF}^{(0)}$, we calculate the dependence of the ratio R_1 on the hole density or on the doping; we consider also the influence of the disorder on R_1. We compare the theoretical predictions with the experimental results (if the experimental data is known). In one case we plot openly the dependence of the energy gap on the temperature, since the right experimental data has existed in the literature.

In particular, we take under consideration following families of the high-T_C materials:

$YBa_2Cu_3O_{7-y}$ (YBCO) - for selected values of the hole density (p - (holes/Cu)),

$YBa_2Cu_3O_{7-y}$ (YBCO) - the disorder induced by electron irradiation, which results in the creation of point defects such as Cu and O vacancies in the CuO_2 planes,

$YBa_2(Cu_{1-x}Zn_x)_3O_{7-y}$ (Zn-YBCO) - the in-plane disorder caused by zinc,

$Y_{1-x}Pr_xBa_2Cu_3O_{7-y}$ (Pr-YBCO) - the out-of-plane disorder caused by praseodymium,

$NdBa_2(Cu_{1-x}Ni_x)_3O_{7-y}$ (Ni-NdBCO) - for selected values of x and y.

Next, we consider $Bi_2Sr_2CaCu_2O_{8+y}$ (Bi2212) - for selected values of the hole density, and $Bi_2Sr_2Ca_2Cu_3O_{10+y}$ (Bi2223) - for the optimally doped case (OP).

Finally, $Pr_{2-x}Ce_xCuO_{4-y}$ (PCCO) - the example of electron-doped cuprate.

The experimental data and the obtained theoretical results are collected in the Table 1. Mathematically, the range of the Nernst region can be characterized by the quantity: $\Delta^{**} \equiv (T^{**} - T_C)/T_C$. On the basis of experiments, we conclude that the Nernst region strongly expands if the hole density decreases; this is clear to see for YBCO and Bi2212, where $[\Delta^{**}]_{max} = 7.08$ and $[\Delta^{**}]_{max} = 1.18$ respectively; also for underdoped Ni-NdBCO, where $[\Delta^{**}]_{max} = 3$. In the case of the disorder which is induced in YBCO, the value of Δ^{**} considerably increases if the electron irradiation is used or yttrium is substituted by praseodymium; the disorder caused by zinc weakly influences on the value of Δ^{**}. In the presented analysis we consider also the electron-doped cuprate system PCCO for which Δ^{**} increases if doping decreases (from optimally to underdoped region). In overdoped region of PCCO the value of Δ^{**} can not be determined, since T_C and T^{**} are experimentally indistinguishable.

Now, we consider the obtained values of V and $U_{MF}^{(0)}$. We notice that for real materials both V and $U_{MF}^{(0)}$ are significant and the following principle is in effect: if Δ^{**} is smaller than ~ 0.6 we have $V > U_{MF}^{(0)}$, in the opposite case $V < U_{MF}^{(0)}$; the especially high values of $U_{MF}^{(0)}$ can be observed in the strongly underdoped regime.

By using the input parameters presented in Table 1 we compare the calculated theoretical values of the ratio R_1 with the experimental data.

In Fig. 8 we show the ratio R_1 as a function of the hole density for YBCO. The numerical results are denoted by the solid line with the open circles; the experimental data by the black filled symbols (see also Appendix S5 and the Table S1). It can be seen that, from slightly underdoped to overdoped crystals the presented model correctly predicts the values of R_1 (taking under consideration the several approximations which have already been mentioned previously). For $p \in (0.07, 0.135)$ the theoretical values of the ratio R_1 are probably lower than the experimental data. However, the increasing of R_1 with decreasing of the hole concentration is qualitatively correctly predicted. In the case of the strongly underdoped crystals ($p < 0.07$) the toy model suggests very high values of the ratio R_1 which have to be experimentally checked. In the inset in Fig. 8 there is presented the open dependence of the critical temperature on the hole density with help of which the values of p for YBCO have been calculated [77].

In Figs. 9 (A)–(C) for YBCO we presented the influence of the disorder on the value of the ratio R_1. In Fig. 9 (A), the dependence of R_1 on T_C for the disorder induced by electron irradiation is shown. The two values of the hole concentration are considered: $p = 0.098$ and $p = 0.157$. In both cases the growing disorder, which is being manifested by the lowering values of T_C, causes very distinct increase of the ratio R_1. It is possible to observe the similar effect for the case, when the out-of-plane disorder is caused by praseodymium (Fig. 9 (B)). However, the in-plane disorder which is induced by zinc in principle doesn't affect the value of the parameter R_1; see Fig. 9 (C). In Figs. 9 (A)–(C) we have shown only the theoretical predictions, since the experimental data not yet exist.

The dependence of the ratio R_1 on the hole density for Bi2212 is presented in Fig. 10. Similarly as for YBCO, the theoretical results are denoted by the solid line with the open circles and the experimental data by the filled and half-filled symbols (Appendix S5 and the Table S2). Additionally, the region between the dotted lines represents the possible experimental values obtained by using the empirical formula [78]:

$$R_1(p) = (15 \pm 1) - (38 \pm 5)p. \tag{33}$$

We can notice that relation (33) represents the linear least-squares fit to the experimental data and it is valid for $0.12 < p < 0.24$. On the basis of the presented results we conclude, that the toy model, in a wide range of the p values, very correctly reproduces the experimental data. It is possible to have reservation only for very low values of p, where some experimental data suggested extremely high values of the ratio R_1. The inset in Fig. 10 presents the dependence of the energy gap on the temperature for Bi2212 with $T_C = 67$ K. In particular, the region between the solid lines corresponds to the possible theoretical values of Δ_{tot}. Let us notice that theoretical results were set with the experimentally accuracy of T^{**} (see also the Table 1). In the inset we also show the experimental data obtained by A. Kanigel, *et al.* [79]. It is easy to see that the agreement between theoretical and experimental results is excellent.

However, for Bi2223 and Ni-NdBCO superconductors the values of t and ω_0 are unknown and we take t and ω_0 for Bi2212 and YBCO respectively, it is possible to receive good estimating of the real values of R_1. In the case of Bi2223 we have $R_1 = 8.01$. On the basis of the results presented in Appendix S5 and the Table S3 we see that our theoretical value is very close to the experimental

Table 1. The quantities δ^{**}, V and $U_{MF}^{(0)}$ calculated by using the mean values of T_C and T^{**}.

Material	Type	t	Ref.	ω_0	Ref.	T_C	T^{**}	Ref.	δ^{**}	V	$U_{MF}^{(0)}$
		meV		meV		K	K			t	t
YBCO	$p=0.062$	250	[59]	75	[33]	18.6	150.2	[121]	**7.08**	**0.838**	**2.847**
	$p=0.079$					45	128.3		**1.85**	**1.148**	**2.045**
	$p=0.107$					60.5	91.8		**0.52**	**1.297**	**1.171**
	$p=0.116$					64.1	84.9		**0.32**	**1.330**	**0.969**
	$p=0.120$					66.5	87.4		**0.31**	**1.352**	**0.974**
	$p=0.138$					80.6	104.4		**0.30**	**1.475**	**1.062**
	$p=0.150$					90	105		**0.17**	**1.554**	**0.898**
	$p=0.176$					92	107	[76]	**0.16**	**1.571**	**0.903**
$YBCO_e$	$p=0.098$	250	[59]	75	[33]	57	85	[122]	**0.49**	**1.265**	**1.104**
	$p=0.098$					45.1	83.1		**0.84**	**1.150**	**1.288**
	$p=0.098$					24.2	75		**2.10**	**0.915**	**1.564**
	$p=0.157$					92.6	103		**0.11**	**1.576**	**0.796**
	$p=0.157$					79.5	97.1		**0.22**	**1.465**	**0.930**
	$p=0.157$					48.6	82.5		**0.70**	**1.184**	**1.213**
Zn-YBCO	x = 0.000	250	[59]	75	[33]	90	104 ± 5	[123]	**0.16**	**1.554**	**0.876**
	x = 0.005					84	96 ± 5		**0.14**	**1.504**	**0.813**
	x = 0.010					79	87 ± 5		**0.10**	**1.461**	**0.700**
	x = 0.020					67	75 ± 5		**0.12**	**1.356**	**0.674**
Pr-YBCO	x = 0.0	250	[59]	75	[33]	89.7	104.8 ± 5	[124]	**0.17**	**1.552**	**0.899**
	x = 0.1					83.8	99.9 ± 5		**0.19**	**1.502**	**0.908**
	x = 0.2					68.2	95 ± 5		**0.39**	**1.367**	**1.096**
	x = 0.3					50.2	84.8 ± 5		**0.69**	**1.200**	**1.226**
	x = 0.4					40.7	79.9 ± 5		**0.96**	**1.104**	**1.313**
Ni-NdBCO	x = 0.00,y = 0.0	250	–	75	–	95	115 ± 20^a	[125]	**0.21**	**1.596**	**1.021**
	x = 0.03,y = 0.0					59 ± 4	80 ± 20^a		**0.36**	**1.283**	**0.966**
	x = 0.06,y = 0.0					45 ± 5	65 ± 20^a		**0.44**	**1.148**	**0.940**
	x = 0.00,y = 0.2					53 ± 3.5	75 ± 5		**0.42**	**1.227**	**0.981**
	x = 0.03,y = 0.2					20 ± 7	80 ± 10		**3.00**	**0.858**	**1.737**
Bi2212	$p=0.087$	350	[126],[127],	80	[29],[30],	50	108.9 ± 5	[76],[128].	**1.18**	**1.117**	**1.508**
	$p=0.118$		[129]		[31],[130],	77.9	130.3 ± 10		**0.67**	**1.347**	**1.442**
	$p=0.160$				[131].	90.6	125.4 ± 5		**0.38**	**1.444**	**1.184**
	$p=0.202$					76.9	105.5 ± 5		**0.37**	**1.339**	**1.050**
	$p=0.219$					64.9	85.5 ± 10		**0.32**	**1.243**	**0.888**
Bi2223	OP	350	–	80	–	109	135	[76]	**0.24**	**1.580**	**1.077**
PCCO	x = 0.13	380	[60],[61],	33	[132],[133].	12 ± 1	18 ± 1	[134]	**0.50**	**0.795**	**0.715**
	x = 0.14		[135],[136].			19.5 ± 1	23 ± 1		**0.18**	**0.947**	**0.529**
	x = 0.15					20 ± 1	22 ± 1		–	**0.956**	0.174
	x = 0.17					13 ± 1	13.5 ± 1		–	**0.817**	0.002
	x = 0.19					6.5 ± 1	7 ± 1		–	**0.654**	$\sim 0^b$

For YBCO the hole density p is estimated from the relation presented in [77]; for Bi2212 from the empirical formula $T_C(p)/T_{C,max}=1-82.6(p-0.16)^2$ [120]. For the superconductors Ni-NdBCO and Bi2223 the values of t and ω_0 are unknown. In this case, we take t and ω_0 for YBCO and Bi2212 respectively.

[a]The high value of the experimental error.

[b]The value found based on $[R_1]_{exp}$.

doi:10.1371/journal.pone.0031873.t001

data. For Ni-NdBCO the situation is more complicated. If we consider Ni-NdBCO superconductor with y = 0 the experimental error for T^{**} is too big, so it is impossible exactly determine R_1. However, if we take the mean values of T_C and T^{**} the theoretical results indicate that the ratio R_1 has the values 7.97, 10.20, 11.78 respectively for x = 0, x = 0.03 and x = 0.06. We notice that the experimental value of R_1 for x = 0 is equal to 7.3 (see Appendix S5 and the Table S4). For the case y = 0.2 the experimental data are much more accurate and we have R_1 equal to $10.98^{+1.69}_{-1.65}$ and $32.90^{+21.43}_{-10.68}$ for x = 0 and x = 0.03 respectively. On the basis of

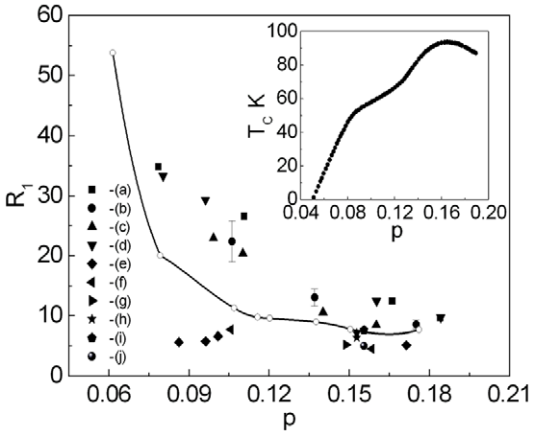

Figure 8. The dependence of the ratio R_1 on p for YBCO. The solid line with the open circles represents the theoretical calculation. The black filled symbols correspond to experimental results obtained by: (a) - M. Sutherland *et al.* [84], (b) - K. Nakayama *et al.* [85], (c) - A. Kaminski *et al.* [86], (d) - M. Plate *et al.* [87], (e) - D.K. Morr *et al.* [88], H.F. Fong *et al.* [89], (f) - N.C. Yeh *et al.* [90], (g) - V. Born *et al.* [91], (h) - H. Murakami *et al.* [92], (i) - H. Edwards *et al.* [93], (j) - H. Edwards *et al.* [94]. The inset shows the dependence of the critical temperature on the hole density estimated from the relation presented in [77].
doi:10.1371/journal.pone.0031873.g008

above results we see that the last value of the ratio R_1 can be extraordinary big (this result should be checked experimentally).

The general phase diagram of the high-T_C superconductors presents the global symmetry between the hole- and electron-doped materials [80]. First of all, in both cases, the antiferromagnetic phase has the similar Neel temperature (however for electron-doped cuprates, the antiferromagnetic phase is broader). Secondly, the superconducting phase for the hole- and electron-doped materials appears closely to antiferromagnetic phase, with the similar value of the optimal doping ($x \sim 0.16$). The distinct symmetry of the phase diagram strongly supports the view that the hole- and electron-doped superconductors should have an

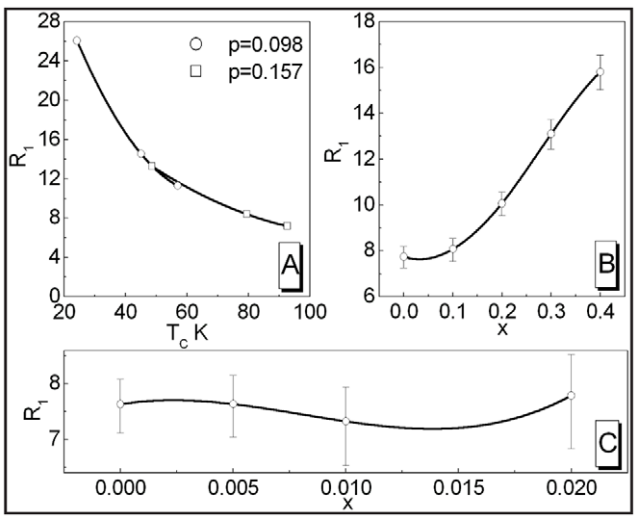

Figure 9. (*A*) The dependence of the ratio R_1 on T_C for $YBCO_e$; we consider the case $p=0.098$ and $p=0.157$. (*B*) The dependence of the ratio R_1 on x for Pr-YBCO. (*C*) The dependence of the ratio R_1 on x for Zn-YBCO.
doi:10.1371/journal.pone.0031873.g009

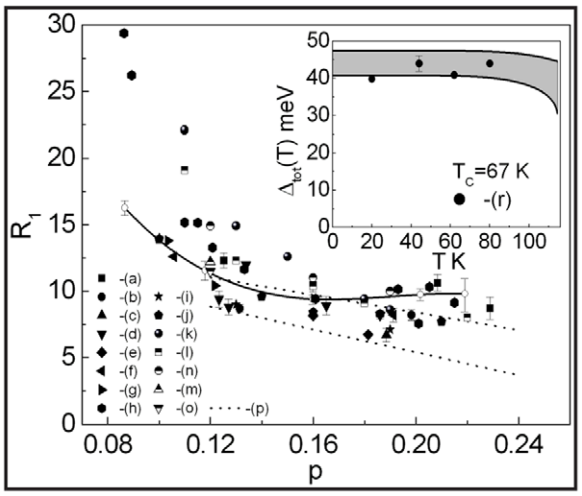

Figure 10. The dependence of the ratio R_1 on p for Bi2212. The solid line with the open circles represents the theoretical calculation. The filled and half-filled symbols correspond to experimental results obtained by: (a) - Ch. Renner, *et al.* [74], [75], (b) - A. Hoffmann, *et al.* [95], (c) - Y.G. Ponomarev, *et al.* [96], (d) - T. Oki, *et al.* [97], (e) - V.M. Krasnov, *et al.* [98], (f) - A.K. Gupta, *et al.* [99], (g) - A. Kanigel, *et al.* [79], (h) - J.C. Campuzano, *et al.* [100], K. Tanaka, *et al.* [101], (i) - T. Nakano, *et al.* [102], (j) - M. Oda, *et al.* [103], (k) - K. McElroy, *et al.* [104], (l) - A. Matsuda, *et al.* [105], (m) - J.E. Hoffman, *et al.* [106], (n) - C. Howald, *et al.* [107], (o) - H. Murakami, *et al.* [108]. The lines (p) are obtained by using the empirical relation (33). The inset shows the dependence of the energy gap on the temperature; the filled region between the solid lines represents possible theoretical values of Δ_{tot}; (r) - the experimental results [79].
doi:10.1371/journal.pone.0031873.g010

identical pairing mechanism. For that reason, the analysis of R_1 for the selected electron-doped superconductor in the framework of toy model is very important.

In Fig. 11 we show the dependence of the ratio R_1 on doping for PCCO. The solid line with open circles represents the theoretical

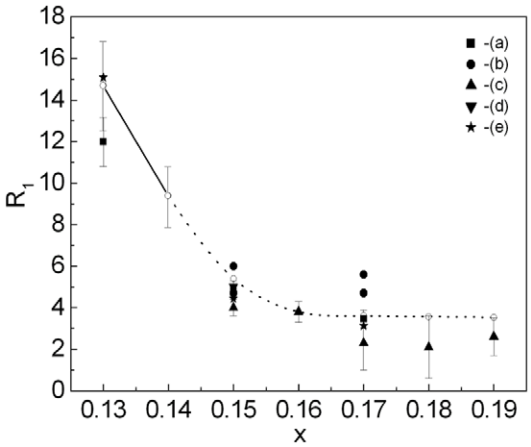

Figure 11. The dependence of the ratio R_1 on x for PCCO. The solid line with the open circles represents the theoretical calculation based on T_C and T^{**}; the dotted line with open circles represents the theoretical calculation based on T_C and the appropriately selected $U_{MF}^{(0)}$. The black filled symbols correspond to experimental results obtained by: (a) - A. Biswas, *et al.* [109], (b) - A. Zimmers, *et al.* [110], (c) - Y. Dagan, *et al.* [111], (d) - C.C. Homes, *et al.* [112], (e) - P. Fournier, *et al.* [113].
doi:10.1371/journal.pone.0031873.g011

calculation obtained by using the input parameters T_C and T^{**}; the dotted line with open circles represents the theoretical calculation obtained by using the input parameters T_C and the appropriately selected $U_{MF}^{(0)}$. The black filled symbols correspond to experimental data (Appendix S5 and the Table S5). Based on Fig. 11, it is easy to see that the theoretical results very well reconstruct the experimental values of R_1.

The Anisotropic Superconductivity

In the presented subsection we will study the thermodynamic properties of the *d*-wave superconducting state on the basis of the postulated pairing model. In particular, we will calculate the dependence of the energy gap amplitude Δ_{tot} on the temperature for the selected values of the EEPH potential. Next, we will analyze the dependence of the $2\Delta_{tot}^{(0)}/k_BT_C$ ratio on the hole density for $La_{2-x}Sr_xCuO_4$ (LSCO) and Bi2212 superconductors. The theoretical predictions will be compared with the experimental data.

Model. The effective Hamiltonian we have rewritten in the form:

$$H \equiv H^{(0)} + H^{(1)} + H^{(2)}. \tag{34}$$

The first term represents the non-interacting electrons:

$$H^{(0)} \equiv \sum_{\mathbf{k}\,\sigma} \varepsilon_{\mathbf{k}}\, c^{\dagger}_{\mathbf{k}\,\sigma} c_{\mathbf{k}\,\sigma}. \tag{35}$$

The EPH and EEPH interaction terms are given by:

$$H^{(1)} \equiv \sum_{\mathbf{k}\,\mathbf{q}\,\sigma} V_{\mathbf{k}\,\mathbf{q}}\, c^{\dagger}_{\mathbf{k}+\mathbf{q}-\sigma} c^{\dagger}_{-\mathbf{k}-\mathbf{q}\,\sigma} c_{-\mathbf{k}\,\sigma} c_{\mathbf{k}\,-\sigma}, \tag{36}$$

and

$$H^{(2)} \equiv \sum_{\mathbf{k}\,\mathbf{k}'\mathbf{q}\,\mathbf{l}\,\sigma} U_{\mathbf{k}\,\mathbf{k}'\mathbf{q}\,\mathbf{l}}\, c^{\dagger}_{\mathbf{k}-\mathbf{l}\,\sigma} c_{\mathbf{k}\,\sigma} h_{\mathbf{k}'\mathbf{l}\mathbf{q}\,\sigma} c^{\dagger}_{-\mathbf{k}+\mathbf{l}-\sigma} c_{-\mathbf{k}-\sigma}, \tag{37}$$

where: $h_{\mathbf{k}'\mathbf{l}\mathbf{q}\,\sigma} \equiv c^{\dagger}_{\mathbf{k}'+\mathbf{l}+\mathbf{q}-\sigma} c_{\mathbf{k}'-\sigma} c^{\dagger}_{-\mathbf{k}'-\mathbf{l}-\mathbf{q}\,\sigma} c_{-\mathbf{k}'\sigma}$. The functions $V_{\mathbf{k}\mathbf{q}}$ and $U_{\mathbf{k}\mathbf{k}'\mathbf{q}\mathbf{l}}$ indicate the pairing potentials:

$$V_{\mathbf{k}\mathbf{q}} \equiv \frac{\omega_0 |g^{(1)}|^2}{\left(\varepsilon_{\mathbf{k}} - \varepsilon_{\mathbf{k}+\mathbf{q}}\right)^2 - \omega_0^2}, \tag{38}$$

and

$$U_{\mathbf{k}\,\mathbf{k}'\,\mathbf{q}\,\mathbf{l}} \equiv \frac{\omega_0 |g^{(2)}|^2}{\left(\varepsilon_{\mathbf{k}} - \varepsilon_{\mathbf{k}-\mathbf{l}} + \varepsilon_{\mathbf{k}'} - \varepsilon_{\mathbf{k}'+\mathbf{l}+\mathbf{q}}\right)^2 - \omega_0^2}. \tag{39}$$

On the basis of the operators (36) and (37) it is possible to deduce the Hamiltonians which describe the *d*-wave superconducting state. In the case of the Hamiltonian (36) this procedure is known and widely described in the literature (see e.g. the paper [81]). With reference to the above, we will discuss only the derivation of the anisotropic Hamiltonian on the basis of the EEPH operator. In the first step, we separate the momentums in the expression (37):

$$H^{(2)} \simeq \sum_{\mathbf{k}_1 \sim \mathbf{k}_4 \sigma} U_{\mathbf{k}_1 \sim \mathbf{k}_4} c^{\dagger}_{-\mathbf{k}_1\sigma} c_{-\mathbf{k}_2\sigma} h_{\mathbf{k}_3\mathbf{k}_4\sigma} c^{\dagger}_{\mathbf{k}_1-\sigma} c_{\mathbf{k}_2-\sigma}, \tag{40}$$

where: $h_{\mathbf{k}_3\mathbf{k}_4\sigma} \equiv c^{\dagger}_{\mathbf{k}_3-\sigma} c^{\dagger}_{-\mathbf{k}_3\sigma} c_{-\mathbf{k}_4\sigma} c_{\mathbf{k}_4-\sigma}$.

With help of the relation: $c_{\mathbf{k}\sigma} = \frac{1}{\sqrt{N}} \sum_j e^{-i\mathbf{k}\mathbf{R}_j} c_{j\sigma}$, we transform the operator (40) to the Wannier representation, where we restrict ourselves to on-site and the nearest neighbor pairing. The Hamiltonian takes the form:

$$\begin{aligned} H^{(2)} \simeq & \sum_{\langle j_1 j_2\rangle \langle j_3 j_4\rangle \sigma} U^{(-)}_{j_1 \sim j_4} c^{\dagger}_{j_1\sigma} c_{j_1\sigma} h^{(-)}_{j_3 j_4\sigma} c^{\dagger}_{j_2-\sigma} c_{j_2-\sigma} \\ & + \sum_{\langle j_1 j_2\rangle \langle j_3 j_4\rangle \sigma} U^{(+)}_{j_1 \sim j_4} c^{\dagger}_{j_1\sigma} c_{j_2\sigma} h^{(+)}_{j_3 j_4\sigma} c^{\dagger}_{j_2-\sigma} c_{j_1-\sigma}, \end{aligned} \tag{41}$$

where $h^{(-)}_{j_3 j_4\sigma} \equiv c^{\dagger}_{j_3-\sigma} c_{j_3-\sigma} c^{\dagger}_{j_4\sigma} c_{j_4\sigma}$ and $h^{(+)}_{j_3 j_4\sigma} \equiv c^{\dagger}_{j_3-\sigma} c_{j_4-\sigma} c^{\dagger}_{j_4\sigma} c_{j_3\sigma}$. The symbols $U^{(-)}_{j_1 \sim j_4}$ and $U^{(+)}_{j_1 \sim j_4}$ denote the local and kinetic potential respectively. Next, we return to the Bloch representation:

$$\begin{aligned} H^{(2)} \simeq & \sum_{\mathbf{k}_1 \sim \mathbf{k}_4 \sigma} \left[U^{(-)}_{\mathbf{k}_1 \sim \mathbf{k}_4} + U^{(+)}_{\mathbf{k}_1 \sim \mathbf{k}_4} \right] \\ & \times c^{\dagger}_{-\mathbf{k}_1\sigma} c_{-\mathbf{k}_2\sigma} h_{\mathbf{k}_3\mathbf{k}_4\sigma} c^{\dagger}_{\mathbf{k}_1-\sigma} c_{\mathbf{k}_2-\sigma}, \end{aligned} \tag{42}$$

where:

$$\begin{aligned} U^{(\pm)}(\mathbf{k}_1 \sim \mathbf{k}_4) \equiv & \frac{1}{N^4} \sum_{\langle j_1 j_2\rangle} \sum_{\langle j_3 j_4\rangle} U^{(\pm)}_{j_1 \sim j_4} \\ & \times e^{\mp i(\mathbf{k}_2 \pm \mathbf{k}_1)\left(\mathbf{R}_{j_2} - \mathbf{R}_{j_1}\right) \pm i(\mathbf{k}_4 \pm \mathbf{k}_3)\left(\mathbf{R}_{j_4} - \mathbf{R}_{j_3}\right)}. \end{aligned} \tag{43}$$

Now, we assume: $U^{(-)}_{j_1 \sim j_4} \simeq U^{(+)}_{j_1 \sim j_4} = -U/24N_0^3$, where the symbol N_0 denotes the normalization factor: $N_0 \equiv 1/\sum_{\mathbf{k}}^{\omega_0}$. In the next step, we limit the symmetry of the energy gap to the dominating *d*-wave symmetry. The total Hamiltonian after applying the approximation presented for the *s*-wave takes the form:

$$\begin{aligned} H^{(\eta)} \equiv & \sum_{\mathbf{k}\,\sigma} \varepsilon_{\mathbf{k}} c^{\dagger}_{\mathbf{k}\,\sigma} c_{\mathbf{k}\,\sigma} - \left(V^{(\eta)} + \frac{U^{(\eta)}}{6} \left|\Delta^{(\eta)}\right|^2 \right) \\ & \times \sum_{\mathbf{k}}^{\omega_0} \left[\Delta^{(\eta)}_{\mathbf{k}} c^{\dagger}_{\mathbf{k}\uparrow} c^{\dagger}_{-\mathbf{k}\downarrow} + \Delta^{\star(\eta)}_{\mathbf{k}} c_{-\mathbf{k}\downarrow} c_{\mathbf{k}\uparrow} \right]. \end{aligned} \tag{44}$$

The symbol $V^{(\eta)}$ and $U^{(\eta)}$ denotes the *d*-wave effective potential for the EPH and EEPH channel respectively. In particular: $V^{(\eta)} \equiv V/2$ and $U^{(\eta)} \equiv U/8$. The anisotropic order parameter is given by: $\Delta^{(\eta)}_{\mathbf{k}} \equiv \Delta^{(\eta)} \eta(\mathbf{k})$, where the amplitude is expressed as: $\Delta^{(\eta)} \equiv \frac{1}{N_0} \sum_{\mathbf{k}}^{\omega_0} \eta(\mathbf{k}) \langle c_{-\mathbf{k}\downarrow} c_{\mathbf{k}\uparrow} \rangle$ and $\eta(\mathbf{k}) \equiv 2\left[\cos(k_x) - \cos(k_y)\right]$.

On the basis of the Hamiltonian (44), we calculate the thermodynamic Green function by using the equation of motion method. The result has the form:

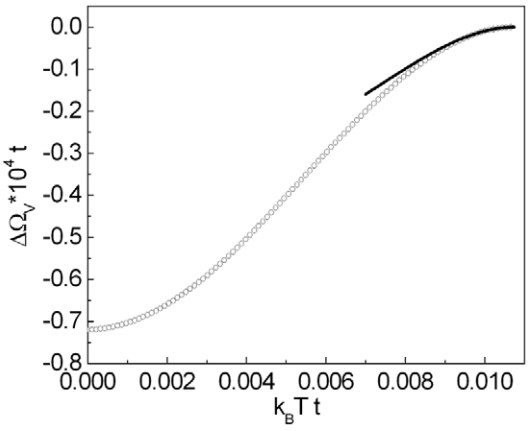

Figure 12. The dependence of the energy gap amplitude on the temperature for the selected values of the EEPH potential. The solid line represents the physical stable solution; the dotted line corresponds to the unstable solution, where the thermodynamic potential is bigger than in the first case. The vertical line indicates the position of the critical temperature.
doi:10.1371/journal.pone.0031873.g012

$$\langle\langle c_{\mathbf{k}\uparrow}|c_{-\mathbf{k}\downarrow}\rangle\rangle = -\frac{\left(V^{(\eta)}+\frac{U^{(\eta)}}{6}\left|\Delta^{(\eta)}\right|^2\right)\Delta_{\mathbf{k}}^{(\eta)}}{\omega^2-\left(E_{\mathbf{k}}^{(\eta)}\right)^2}, \qquad (45)$$

where:

$$E_{\mathbf{k}}^{(\eta)} \equiv \sqrt{\epsilon_{\mathbf{k}}^2+\left(V^{(\eta)}+\frac{U^{(\eta)}}{6}\left|\Delta^{(\eta)}\right|^2\right)^2\left(\left|\Delta^{(\eta)}\right|\eta(\mathbf{k})\right)^2}. \qquad (46)$$

We turn the reader's attention toward the fact, that the obtained Green function possesses the analytical structure, which is more complex than the structure of the BCS Green function [56], [57] [82]. In particular, the energy gap amplitude is the complicated function of the order parameter amplitude. However, the energy gap, in spite of its complicated form, is characterized by the pure *d*-wave symmetry.

On the basis of Eq. (45) we derive the fundamental thermodynamic equation:

$$1=\left(V^{(\eta)}+\frac{U^{(\eta)}}{6}\left|\Delta^{(\eta)}\right|^2\right)\frac{1}{N_0}\sum_{\mathbf{k}}^{\omega_0}\frac{\eta^2(\mathbf{k})}{2E_{\mathbf{k}}^{(\eta)}}\tanh\frac{\beta E_{\mathbf{k}}^{(\eta)}}{2}. \qquad (47)$$

The sum $\sum_{\mathbf{k}}^{\omega_0}$ is approximated in the following manner: $\sum_{\mathbf{k}}^{\omega_0} \simeq \int_{-\pi}^{\pi}\int_{-\pi}^{\pi} dk_x dk_y \theta\left(\omega_0-|\varepsilon_{k_x,k_y}|\right)$, where the symbol θ represents the unit step function. In the model calculations, we have taken t as the energy unit.

The numerical results. In Fig. 12 we present the temperature dependence of the energy gap amplitude. $(\Delta_{tot}\equiv\left(V^{(\eta)}+\frac{U^{(\eta)}}{6}\left|\Delta^{(\eta)}\right|^2\right)\left|\Delta^{(\eta)}\right|)$ for $V^{(\eta)}=0.02t,\ \omega_0=0.3t$ and the selected values of $U^{(\eta)}$. It is easy to see, that for the high values of the EEPH potential, the shape of the function $\Delta_{tot}(T)$ is sharply different from the BCS prediction. In particular, for $T\in<0,T_C>$ the energy gap is very weakly dependent on the temperature; up to the critical temperature Δ_{tot} extends into the anomalous normal state to the temperature T^*. In the case of the *d*-wave superconducting state, the temperature T^* is interpreted as the pseudogap temperature (in contrast to the *s*-wave superconductivity, where the highest value of the temperature, for which the non-zero solution of the gap equation exists, is connected with the Nernst temperature T^{**}).

Below we compare the theoretical predictions with the experimental data for LSCO and Bi2212 superconductors. For this purpose, we have calculated the values of the pairing potentials on the basis of T_C and T^* experimental values. The obtained results have been collected in Table 2. Next, by using the $V^{(\eta)}$ and $U^{(\eta)}$ values, the hole density dependence of the $R_1\equiv 2\Delta_{tot}^{(0)}/k_BT_C$ ratio has been obtained. We notice, that the energy gap amplitude at the temperature of zero Kelvin is defined as: $\Delta_{tot}^{(0)}\equiv\left(V^{(\eta)}+\frac{U^{(\eta)}}{6}\left|\Delta_0^{(\eta)}\right|^2\right)\left|\Delta_0^{(\eta)}\right|$, where $\Delta_0^{(\eta)}$ denotes the order parameter amplitude at the temperature of zero Kelvin.

In Fig. 13 we present the dependence of the R_1 ratio on the hole density for LSCO superconductor. It can be seen, that with the increase of p, the parameter R_1 successively decreases. In particular, for the underdoped region ($p<0.155$) the values of R_1 are significantly higher than the *d*-wave BCS value 4.28 [83]. Slightly above $p=0.155$ (the overdoped region) the R_1 ratio approaches closely the weak-coupling *d*-wave BCS result. We notice, that for $p>0.15$, the lower accuracy of the theoretical results can not be determined, since T_C and T^* are experimentally indistinguishable (see Table 2). Now, we have compared the

Table 2. The parameters $V^{(\eta)}$ and $U^{(\eta)}$ calculated by using T_C and the mean values of T^*.

Material	Type	t	Ref.	ω_0	Ref.	T_C	T^*	Ref.	$V^{(\eta)}$	$U^{(\eta)}$
		meV		meV		K	K		meV	meV
LSCO	$p=0.10^a$	240	[58]	96	[13]	58	193.7 ± 30.2	[114]	**3.76**	**66.86**
	$p=0.15^a$					38	135.5 ± 30.2	[114]	**4.41**	**53.89**
	$p=0.22^a$					28	44.3 ± 30.2	[114]	**3.91**	**45.11**
Bi2212	$p=0.125$	350	[126],[127],	80	[29],[30],	83	~290	[74],[75]	**5.47**	**55.40**
	$p=0.143$		[129].		[31],[130],	90	~300	[137]	**5.68**	**56.37**
	$p=0.193$				[131].	84	~270	[137]	**5.51**	**51.72**
	$p=0.198$					81	~220	[137]	**5.40**	**43.88**

[a]The hole density p has been estimated as the doping $p=x$.
doi:10.1371/journal.pone.0031873.t002

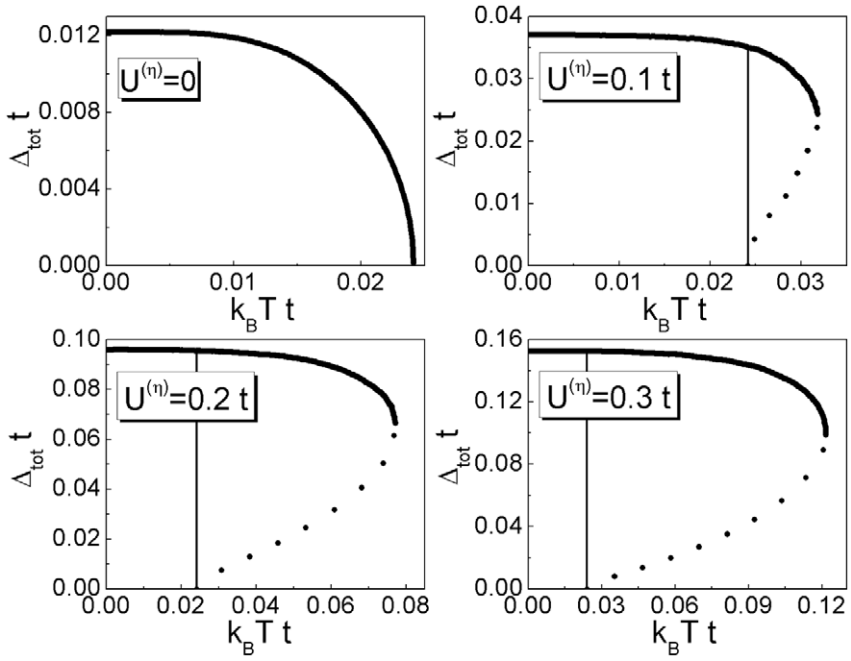

Figure 13. The ratio R_1 as a function of p for LCSO superconductor. The solid lines with the open squares represent the theoretical calculations based on the data presented in the paper [114]. The overshadowed areas mean the accuracy of the achieved results. The filled symbols correspond to the experimental results obtained by: (a) - Hashimoto, *et al.* [114], (b) - Nakano, *et al.* [102], (c) - Oda, *et al.* [115], (d) - Kato, *et al.* [116], (e) - Wang, *et al.* [117], (f) - Yoshida, *et al.* [118], (g) - Wen, *et al.* [119].
doi:10.1371/journal.pone.0031873.g013

theoretical predictions which the experimental values of R_1, received by the few different researchers. The qualitative agreement of the theoretical predictions with the experimental data proves, that the measured dependence of the ratio R_1 on p can be well reproduced with an use of the presented model.

In Fig. 14 we show the shape of the function $R_1(p)$ for Bi2212 superconductor. The presented results prove, that the theoretical line determines the high value of R_1 in the whole range of the considered hole density; $p \in <0.125,198>$. Important is also the fact, that the model correctly reconstructs the experimental data.

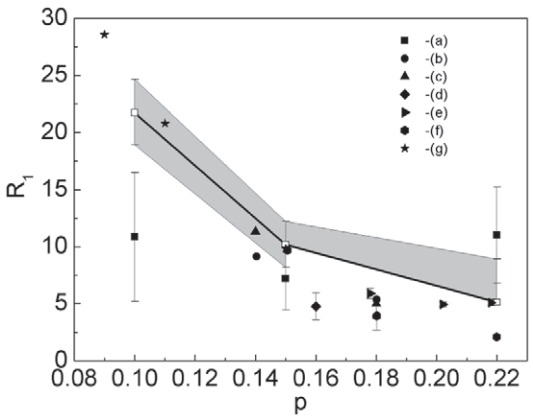

Figure 14. The dependence of the ratio R_1 on p for Bi2212. The solid line with the open squares represents the theoretical calculation. The filled and half-filled symbols correspond to the experimental results obtained by: (a) - Renner, *et al.* [74], [75], (b) - Hoffmann, *et al.* [95], (c) - Ponomarev, *et al.* [96], (d) - Oki, *et al.* [97], (e) - Krasnov, *et al.* [98], (f) - Gupta, *et al.* [99], (g) - Kanigel, *et al.* [79], (h) - Campuzano, *et al.* [100], Tanaka, *et al.* [101], (i) - Nakano, *et al.* [102], (j) - Oda, *et al.* [103], (k) - McElroy, *et al.* [104], (l) - Matsuda, *et al.* [105], (m) - Hoffman, *et al.* [106]. The lines (n) are obtained by using the empirical relation (33).
doi:10.1371/journal.pone.0031873.g014

Discussion

In the paper the microscopic model of the superconducting state that induces at high temperature was presented. The starting point of our considerations was the assumed statement: that a proper description of the superconducting condensate in the cuprates is possible only when the pairing mechanism would *inseparably* link together the strong electron correlations and the crystal lattice vibrations. The Hamiltonian proposed in the paper seems to be the most simple among the operators that satisfy the above postulate.

In the study we have shown, that for the large values of the EEPH coupling, the *s*-wave energy gap at the vicinity of the superconducting state existence weakly depends on the temperature and it vanishes above T_C (at the temperature that was interpreted as Nernst temperature). The key test of our model was the determination of the dependence of the ratio R_1 on doping for the selected superconductors. The obtained agreement between the theoretical and experimental data seems to be extraordinary, when taking into account the simplicity of the considered Hamiltonian and used approximations.

In the paper, we have also presented the model that describes the properties of the *d*-wave superconducting state in the two-dimensional system. In the first step, we have derived the fundamental thermodynamic equation. Next, on the basis of the exact numerical solution, we have shown, that for the high value of the EEPH potential, the temperature dependence of the energy gap amplitude differs sharply from the BCS prediction. In particular, the energy gap is slightly dependent on the temperature for $T \in <0,T_C>$; above the critical temperature, the energy gap persists to the pseudogap temperature. The theoretical predictions

have been compared with the experimental data for LCSO and Bi2212 superconductors. It has been shown, that the calculated hole density dependence of the R_1 ratio correctly reproduces the experimental data.

In our opinion, the achieved results clearly suggest that presented pairing mechanism should be seriously taken into consideration in the further researches which may lead to the most precise understanding of the properties of the high temperature superconducting state.

Methods

Numerical Calculations

The calculations have been conducted on the Częstochowa University of Technology cluster, built in the framework of the PLATON project, no. POIG.02.03.00-00-028/08 - the service of the campus calculations U3. The Fortran programming language has been used.

Supporting Information

Appendix S1 The formally exact expression for the self-energy matrix.
(PDF)

Appendix S2 The *fold* mean-field approximation.
(PDF)

Appendix S3 The accuracy of the *fold* mean-field approximation in the framework of the random phase approximation (RPA) method.
(PDF)

Appendix S4 The van Hove and generalized mean-field thermodynamic potential.
(PDF)

Appendix S5 The lists of the experimental values of the thermodynamic parameters for the selected high-T_C superconductors.
(PDF)

Figure S1 The dependence of $\Delta\Omega_V$ on the temperature. We assume $V=1t$ and $\omega_0=0.3t$. The empty circles are obtained from Eq. (8) with help of Eqs. (9) and (14). Solid line represents the calculation of $\Delta\Omega_V$ using the formula (16). We notice that the equations have been taken from the Appendix S4.
(EPS)

Table S1 The experimental data for YBa2Cu3O7−y (YBCO).
(PDF)

Table S2 The experimental data for Bi2Sr2CaCu2O8+y (Bi2212).
(PDF)

Table S3 The experimental data for Bi2Sr2Ca2-Cu3O10+y (Bi2223).
(PDF)

Table S4 The experimental data for NdBa2Cu3O7−y (NdBCO).
(PDF)

Table S5 The experimental data for Pr2−xCexCuO4−y (PCCO).
(PDF)

Acknowledgments

The author wishes to thank Prof. K. Dziliński, the Head of the Institute of Physics at Częstochowa University of Technology, for providing excellent working conditions. Additionally, I would like to thank my colleagues and students: D. Szczęśniak, M.W. Jarosik, A.P. Durajski and T. Mila for their kindness during the preparation of this work.

Author Contributions

Analyzed the data: RSZ. Wrote the paper: RSZ. Conceived and designed the model: RSZ. Performed the analytical calculations: RSZ. Performed the numerical calculations: RSZ.

References

1. Bednorz JG, Müller KA (1986) Possible high t_C superconductivity in the ba-la-cu-o system. Z Phys B 64: 189–193.
2. Bednorz JG, Müller KA (1988) Perovskite-type oxides – the new approach to high-t_C superconductivity. Rev Mod Phys 60: 585–600.
3. Dagotto E (1994) Correlated electrons in high-temperature superconductors. Rev Mod Phys 66: 763–841.
4. Hubbard J (1963) Electron correlations in narrow energy bands. Proc R Soc London, Ser A 276: 238–257.
5. Emery VJ (1987) Theory of high-t_C superconductivity in oxides. Phys Rev Lett 58: 2794–2797.
6. Littlewood PB, Varma CM, Abrahams E (1989) Pairing instabilities of the extended hubbard model for cu-obased superconductors. Phys Rev Lett 60: 2602–2605.
7. Anderson PW (1987) The resonating valence bond state in *la2cuo*4 and superconductivity. Science 235: 1196–1198.
8. Lee PA, Nagaosa N, Wen CG (2006) Doping a mott insulator: Physics of high-temperature superconductivity. Rev Mod Phys 78: 17–85.
9. Millis AJ, Monien H, Pines D (1990) Phenomenological model of nuclear relaxation in the normal state of *yba2cu3o7*. Phys Rev B 42: 167–178.
10. Monthoux P, Pines D (1992) Spin-fluctuation-induced superconductivity in the copper oxides: A strong coupling calculation. Phys Rev Lett 69: 961–964.
11. Radtke RJ, Levin K, Schuttler HB, Norman MR (1993) Role of van hove singularities and momentum-space structure in high-temperature superconductivity. Phys Rev B 48: 15957–15965.
12. Chao KA, Spa lek J, Oleś AM (1977) Kinetic exchange interaction in a narrow s-band. J Phys C: Solid State Phys 10: L271–L276.
13. Kim JH, Tesanovic Z (1993) Effects of strong coulomb correlations on the phonon-mediated superconductivity: A model inspired by copper oxides. Phys Rev Lett 71: 4218–4221.
14. Kulic ML (2003) Electron-phonon interaction and strong correlations in high-temperature superconductors: One can not avoid the unavoidable. AIP Conference Proceedings 715: 75–158.
15. Kulic ML (2006) Importance of the electron-phonon interaction with the forward scattering peak for superconducting pairing in cuprates. J Supercond Nov Magn 19: 213–249.
16. Hybertsen MS, Stechel EB, Schluter M, Jennison DR (1990) Renormalization from densityfunctional theory to strong-coupling models for electronic states in cu-o materials. Phys Rev B 41: 11068–11072.
17. Imada M, Hatsugai Y (1989) Numerical studies on the hubbard model and the t-j model in oneand two-dimensions. J Phys Soc Jpn 58: 3752–3780.
18. Imada M (1991) Superconducting correlationof two-dimensional hubbard model near half-filling. J Phys Soc Jpn 60: 2740–2747.
19. Scalapino DJ, White SR, Zhang SC (1992) Superfluid density and the drude weight of the hubbard model. Phys Rev Lett 68: 2830–2833.
20. Hirsch JE (1993) Inapplicability of the hubbard-model for the description of real strongly correlated electrons. Physica B 199: 366–372.
21. Pryadko L, Kivelson S, Zachar O (2004) Incipient order in the $t-j$ model at high temperatures. Phys Rev Lett 92: 067002–1–067002–4.
22. Franck JP (1994) Physical Properties of High Temperature Superconductors. Singapore: World Scientific.
23. Kulic ML (2000) Interplay of electron-phonon interaction and strong correlations: the possible way to high-temperature superconductivity. Phys Rep 338: 1–264.
24. Vedeneev SI, Jansen AGM, Tsvetkov AA, Wyder P (1995) Bloch-gruneisen behavior for the inplane resistivity of *bi2sr2cuo*$_x$ single crystals. Phys Rev B 51: 16380–16383.
25. Tsuei CC, Kirtley JR, Rupp M, Sun JZ, Gupta A, et al. (1996) Pairing symmetry in single-layer tetragonal *tl2ba2cuo*$_{+\delta}$ superconductors. Science 271: 329–332.
26. Tsuei CC, Kirtley JR, Ren ZF, Wang JH, Raffy H, et al. (1997) Pure dx_2-y_2 order-parameter symmetry in the tetragonal superconductor *ti2ba2cuo*$_{6+}$. Nature 387: 481–483.

27. Hofer J, Conder K, Sasagawa T, meng Zhao G, Willemin M, et al. (2000) Oxygen-isotope effect on the in-plane penetration depth in underdoped $la_{2-x}sr_xcuo_4$ single crystals. Phys Rev Lett 84: 4192–4195.
28. Schneider T (2005) Relationship between and implications of the isotope and pressure effects on transition temperature, penetration depths and conductivities. Phys Stat Sol (b) 242: 58–77.
29. Damascelli A, Hussain Z, Shen ZX (2003) Angle-resolved photoemission studies of the cuprate superconductors. Rev Mod Phys 75: 473–541.
30. Cuk T, Lu DH, Zhou XJ, Shen ZX, Deveraux TP, et al. (2005) A review of electron-phonon coupling seen in the high-tC superconductors by angle-resolved photoemission studies (arpes). Phys Stat Sol (b) 242: 11–29.
31. Gweon GH, Sasagawa T, Zhou SY, Graf J, Takagi H, et al. (2004) An unusual isotope effect in a high-transition-temperature superconductor. Nature 430: 187–190.
32. Heid R, Zeyher R, Manske D, Bohnen KP (2009) Phonon-induced pairing interaction in $yba_2cu_3o_7$ within the local-density approximation. Phys Rev B 80: 024507–1–024507–6.
33. Bohnen KP, Heid R, Krauss M (2003) Phonon dispersion and electron-phonon interaction for from first-principles calculations. Europhys Lett 64: 104–110.
34. van Hove L (1953) The occurrence of singularities in the elastic frequency distribution of a crystal. Phys Rev 89: 1189–1193.
35. Markiewicz RS (1997) A survey of the van hove scenario for high-t_C superconductivity with special emphasis on pseudogaps and striped phases. J Phys Chem Sol 58: 1179–1310.
36. Fröhlich H (1950) Theory of the superconducting state. 1. the ground state at the absolute zero of temperature. Phys Rev 79: 845–856.
37. Fröhlich H (1954) On the theory of superconductivity: The one-dimensional case. Proc R Soc A 223: 296–305.
38. Hirsch JE (2001) Dynamic hubbard model. Phys Rev Lett 87: 206402–1–206402–4.
39. Hirsch JE (2002) Quasiparticle undressing in a dynamic hubbard model: Exact diagonalization study. Phys Rev B 66: 064507–1–064507–12.
40. Marsiglio F, Teshima R, Hirsch JE (2003) Dynamic hubbard model: Effect of boson frequency. Phys Rev B 68: 224507–1–224507–7.
41. Lang IG, Firsov YA (1963) Kinetic theory of semiconductors with low mobility. Soviet Physics JETP-USSR 16: 1301–1312.
42. Eliashberg GM (1960) Interactions between electrons and lattice vibrations in a superconductor. Soviet Physics JETP-USSR 11: 696–702.
43. Allen PB, Mitrović B (1982) Solid State Physics: Advances in Research and Applications. New York: Academic.
44. Carbotte JP (1990) Properties of boson-exchange superconductors. Rev Mod Phys 62: 1027–1157.
45. Carbotte JP, Marsiglio F (2003) The Physics of Superconductors. Berlin: Springer.
46. Szczęśniak R (2006) The numerical solution of the imaginary-axis eliashberg equations. Acta Phys Pol A 109: 179–186.
47. Szczęśniak R (2007) On the coulomb pseudopotential for al and pb superconductors. Phys Stat Sol (b) 244: 2538–2542.
48. Szczęśśniak R (2008) The thermodynamic properties of the mgb_2 superconductor: The two-band eliashberg equations. Solid State Commun 145: 137–142.
49. Szczęśniak R, Jarosik MW (2009) The superconducting state in metallic hydrogen under pressure at 2000 gpa. Solid State Commun 149: 2053–2057.
50. Szczęśniak R (2009) Sdw antiferromagnetic phase in the two-dimensional hubbard model: Eliashberg approach. Phys Lett A 373: 473–479.
51. Szczęśniak R, Jarosik MW, Szczęśniak D (2010) Pressure-induced superconductivity in the fcc phase of lithium: Strong-coupling approach. Physica B 405: 4897–4902.
52. Szczęśniak R, Jarosik MW (2011) Properties of the superconducting state in molecular metallic chydrogen under pressure at 347 gpa. Physica B 406: 2235–2239.
53. Szczęśniak R, Jarosik MW (2011) Specific heat and thermodynamic critical field for the molecular metallic hydrogen. Physica B 406: 3493–3497.
54. Szczęśniak R, Durajski AP (2012) Superconductivity of calcium in phase vi. Physica C 472: 15–20.
55. Szczęśniak R, Durajski AP (2012) Thermodynamics of the superconducting state in calcium at 200 gpa. J Supercond Nov Magndoi:10.1007/s10948–011–1326-y.
56. Bardeen J, Cooper LN, Schrieffer JR (1957) Microscopic theory of superconductivity. Phys Rev 106: 162–164.
57. Bardeen J, Cooper LN, Schrieffer JR (1957) Theory of superconductivity. Phys Rev 108: 1175–1204.
58. Xu JH, Watson-Yang TJ, Yu J, Freeman AJ (1987) Dominant role of the 2d van hove singularity on the fermi surface and generalized susceptibility of the quasi-2d superconductor $la_{2-x}m_xcuo_4$ (m = sr, ba, …). Phys Lett A 120: 489–493.
59. Nunner TS, Schmalian J, Bennemann KH (1999) Influence of electron-phonon interaction on spin-fluctuation-induced superconductivity. Phys Rev B 59: 8859–8868.
60. Andersen OK, Liechtenstein AI, Jepsen O, Paulsen F (1995) Lda energy bands, low-energy hamiltonians, t', t'', $t(k)$, and j. J Phys Chem Solids 56: 1573–1591.
61. Lin J, Millis AJ (2005) Theory of low-temperature hall effect in electron-doped cuprates. Phys Rev B 72: 214506–1–214506–9.
62. Hauge JP (2006) Extending the theory of phonon-mediated superconductivity in quasi-2d. AIP Conference Proceedings 846: 255–264.
63. Szczęśniak R, Mierzejewski M, Zieliński J, Entel P (2001) Modification of the isotope effect by the van hove singularity of electrons on a two-dimensional lattice. Solid State Commun 117: 369–371.
64. Szczęśniak R, Grabiński S (2002) The van hove singularity and two-dimensional superconductivity. exact analytical results. Acta Phys Pol A 102: 401–407.
65. Szczęśniak R, Dyga M (2003) The van hove singularity and two-dimensional charge density waves. exact analytical results. Acta Phys Slov 53: 477–487.
66. Szczęśniak R (2006) The selected thermodynamic properties of the strong-coupled superconductors in the van hove scenario. Solid State Commun 138: 347–352.
67. Czerwonko J (2000) Combined bcs and van hove scenarios: A solvable thermodynamics in halffilled symmetric bands. J Phys Element Part At Nucl (Dubna) 31: 145–149.
68. Czerwonko J (1998) Particle-hole asymmetry in the bcs thermodynamics. Acta Phys Pol B 29: 3885–3906.
69. Goicochea AG (1994) High-temperature superconductivity in the van hove scenario. Phys Rev B 49: 6864–6868.
70. Sarkar S, Basu S, Das AN (1995) Pressure coefficient of the superconducting transition temperature within the van hove scenario. Phys Rev B 52: 12545–12547.
71. Sarkar S, Basu S, Das AN (1995) Role of orthorhombic distortion, second-nearest-neighbor hopping, and coulomb repulsion on the superconducting transition temperature and isotope-shift exponent. Phys Rev B 51: 12854–12856.
72. Sarkar S, Das AN (1996) Specific heat and knight shift of cuprates within the van hove scenario. Phys Rev B 54: 14974–14977.
73. Mamedov TA, de Llano M (1999) Boson-exchange superconductor model with a van hove singularity. Phys Lett A 257: 201–208.
74. Renner C, Revaz B, Genoud JY, Kadowaki K, Fischer O (1998) Pseudogap precursor of the superconducting gap in under- and overdoped $bi_2sr_2cacu_2o_{8+\delta}$. Phys Rev Lett 80: 149–152.
75. Renner C, Revaz B, Kadowaki K, Maggio-Aprile I, Fischer O (1998) Observation of the low temperature pseudogap in the vortex cores of $bi_2sr_2cacu_2o_{8+\delta}$. Phys Rev Lett 80: 3606–3609.
76. Wang Y, Li L, Ong NP (2006) Nernst effect in high-t_C superconductors. Phys Rev B 73: 024510–1–024510–20.
77. Liang R, Bonn DA, Hardy WN (2006) Evaluation of cuo_2 plane hole doping in $yba_2cu_3o_{6+x}$ single crystals. Phys Rev B 73: 180505(R)-1–180505(R)-4.
78. Hewitt KC, Irwin JC (2002) Doping dependence of the superconducting gap in $bi_2sr_2cacu_2o_{8+\delta}$. Phys Rev B 66: 054516–1–054516–9.
79. Kanigel A, Chatterjee U, Randeria M, Norman MR, Souma S, et al. (2007) Protected nodes and the collapse of fermi arcs in high-t_C cuprate superconductors. Phys Rev Lett 99: 157001–1–157001–4.
80. Almasan C, Maple MB (1991) Chemistry of High-Temperature Superconductors. Singapore: World Scientific.
81. Newns DM, Tsuei CC, Pattnaik PC (1995) Van hove scenario for d-wave superconductivity in cuprates. Phys Rev B 52: 13611–13618.
82. Gasser W, Heiner E, Elk K (1999) Greensche Funktionen in Festkörper- und Vielteilchenphysik. Weinheim: VILEY-VCH Verlag GmbH.
83. Won H, Maki K (1994) d-wave superconductor as a model of high-t_C superconductors. Phys Rev B 49: 1397–1402.
84. Sutherland M, Hawthorn DG, Hill RW, Ronning F, Wakimoto S, et al. (2003) Thermal conductivity across the phase diagram of cuprates: Low-energy quasiparticles and doping dependence of the superconducting gap. Phys Rev B 67: 174520–1–174520–11.
85. Nakayama K, Sato T, Terashima K, Arakane T, Takahashi T, et al. (2009) Doping dependence of the gap anisotropy of the high-temperature $yba_2cu_3o_{7-\delta}$ superconductor. Phys Rev B 79: 140503(R)-1–140503(R)-4.
86. Kaminski A, Rosenkranz S, Fretwell HM, Mesot J, Randeria M, et al. (2004) Identifying the background signal in angle-resolved photoemission spectra of high-temperature cuprate superconductors. Phys Rev B 69: 212509–1–212509–4.
87. Plate M, Mottershead JDF, Elfimov IS, Peets DC, Liang R, et al. (2005) Fermi surface and quasiparticle excitations of overdoped $tl_2ba_2cuo_{6+\delta}$. Phys Rev Lett 95: 077001–1–077001–4.
88. Morr DK, Pines D (1998) The resonance peak in cuprate superconductors. Phys Rev Lett 81: 1086–1089.
89. Fong HF, Keimer B, Milius DL, Aksay IA (1997) Superconductivity-induced anomalies in the spin excitation spectra of underdoped $yba_2cu_3o_{6+x}$. Phys Rev Lett 78: 713–716.
90. Yeh NC, Chen CT, Hammer G, Mannhart J, Schmehl A, et al. (2001) Evidence of dopingdependent pairing symmetry in cuprate superconductors. Phys Rev Lett 87: 087003–1–087003–4.
91. Born V, Jooss C, Freyhardt HC (2002) Scanning tunneling spectroscopy of optimally doped and underdoped $yba2cu3ox$ thin films. Physica C 382: 224–232.
92. Murakami H, Asaoka H, Sakai K, Ito T, Tonouchi M (2001) Lt-stm/sts observations on electrical field etched surfaces of $yba_2cu_3o_{7-\delta}$ single crystal. Appl Surf Sci 175–176: 306–311.

93. Edwards HL, Markert JT, de Lozanne AL (1992) Energy gap and surface structure of $yba_2cu_3o_{7-x}$ probed by scanning tunneling microscopy. Phys Rev Lett 69: 2967–2970.
94. Edwards HL, Derro DJ, Barr AL, Markert JT, de Lozanne AL (1995) Spatially varying energy gap in the cuo chains of $yba_2cu_3o_{7-x}$ detected by scanning tunneling spectroscopy. Phys Rev Lett 75: 1387–1390.
95. Hoffmann A, Lemmens P, Winkeler L, Guntherodt G (1995) The pairing mechanism in htsc investigated by electronic raman-scattering. J Low Temp Phys 99: 201–203.
96. Ponomarev YG, Timergaleev NZ, Zabezhaylov AO, Uk KK, Lorenz MA, et al. (2000) Conference Series-Institute of Physics 2: 167.
97. Oki T, Tsuda N, Shimada D (2001) Superconducting energy gap of underdoped and overdoped $bi_2sr_2cacu_2o_8$. Physica C 353: 213–220.
98. Krasnov VM, Yurgens A, Winkler D, Delsing P, Claeson T (2000) Evidence for coexistence of the superconducting gap and the pseudogap in bi-2212 from intrinsic tunneling spectroscopy. Phys Rev Lett 84: 5860–5863.
99. Gupta AK, Ng KW (1998) *ab*-plane tunneling spectroscopy of underdoped $bi_2sr_2cacu_2o_y$. Phys Rev B 58: R8901–R8904.
100. Campuzano JC, Ding H, Norman MR, Fretwell HM, Randeria M, et al. (1999) Electronic spectra and their relation to the (π, π) collective mode in high-t_C superconductors. Phys Rev Lett 83: 3709–3712.
101. Tanaka K, Lee WS, Lu DH, Fujimori A, Fujii T, et al. (2006) Distinct fermi-momentum-dependent energy gaps in deeply underdoped bi2212. Science 314: 1910–1913.
102. Nakano T, Momono N, Oda M, Ido M (1998) Correlation between the doping dependences of superconducting gap magnitude $2\delta_0$ and pseudogap temperature t^* in high-t_C cuprates. J Phys Soc Jpn 67: 2622–2625.
103. Oda M, Hoya K, Kubota R, Manabe C, Momono N, et al. (1997) Strong pairing interactions in the underdoped region of $bi_2sr_2cacu_2o_{8+\sigma}$. Physica C 281: 135–142.
104. McElroy K, Lee DH, Hoffmann JE, Lang KM, Lee J, et al. (2005) Coincidence of checkerboard charge order and antinodal state decoherence in strongly underdoped superconducting $bi_2sr_2cacu_2o_{8+\delta}$. Phys Rev Lett 94: 197005–1–197005–4.
105. Matsuda A, Fujii T, Watanabe T (2003) Gap inhomogeneity, phase separation and a pseudogap in $bi_2sr_2cacu_2o_{8+\delta}$. Physica C 388–389: 207–208.
106. Hoffman JE, Hudson EW, Lang KM, Madhavan V, Eisaki H, et al. (2002) A four unit cell periodic pattern of quasi-particle states surrounding vortex cores in $bi_2sr_2cacu_2o_{8+\delta}$. Science 295: 466–469.
107. Howald C, Fournier P, Kapitulnik A (2001) Inherent inhomogeneities in tunneling spectra of $bi_2sr_2cacu_2o_{8-x}$ crystals in the superconducting state. Phys Rev B 64: 100504(R)-1–100504(R)-4.
108. Murakami H, Aoki R (1995) Observation of multi-stage superconducting gap states in $bi_2sr_2cacu_2o_x$ crystal surface by lt-stm/sts. J Phys Soc Jpn 64: 1287–1292.
109. Biswas A, Fournier P, Qazilbash MM, Smolyaninova VN, Balci H, et al. (2002) Evidence of a *d*- to *s*-wave pairing symmetry transition in the electron-doped cuprate superconductor $pr_{2-x}ce_xcuo_4$. Phys Rev Lett 88: 207004–1–207004–4.
110. Zimmers A, Lobo RM, Bontemps N, Homes CC, Barr MC, et al. (2004) Infrared signature of the superconducting state in $pr_{2-x}ce_xcuo_4$. Phys Rev B 70: 132502–1–132502–4.
111. Dagan Y, Beck R, Greene RL (2007) Dirty superconductivity in the electron-doped cuprate $pr_{2-x}ce_xcuo_{4-\delta}$: Tunneling study. Phys Rev Lett 99: 147004–1–147004–4.
112. Homes CC, Lobo RPSM, Fournier P, Zimmers A, Greene RL (2006) Optical determination of the superconducting energy gap in electron-doped $pr_{1.85}ce_{0.15}cuo_4$. Phys Rev B 74: 214515–1–214515–8.
113. Fournier P, Greene RL (2003) Doping dependence of the upper critical field of electron-doped $pr_{2-x}ce_xcuo_4$ thin films. Phys Rev B 68: 094507–1–094507–9.
114. Hashimoto M, Yoshida T, Tanaka K, Fujimori A, Okusawa M, et al. (2007) Distinct doping dependences of the pseudogap and superconducting gap of $la_{2-x}sr_xcuo_4$ cuprate superconductors. Phys Rev B 75: 140503(R)-1–140503(R)-4.
115. Oda M, Matsuzaki T, Momono N, Ido M (2000) Novel relation between t_C and low-t energy gap $2\delta_0$ in bi2212 and la214: an sts study. Physica C 341: 847–850.
116. Kato T, Morimoto H, Katagiri A, Okitsu S, Sakata H (2003) Scanning tunneling microscopy and spectroscopy on $la_{2-x}sr_xcuo_4$. Physica C 392–396: 221–223.
117. Wang Y, Yan J, Shan L, Wen HH, Tanabe Y, et al. (2007) Weak-coupling *d*-wave bcs superconductivity and unpaired electrons in overdoped $la_{2-x}sr_xcuo_4$ single crystals. Phys Rev B 76: 064512–1–064512–6.
118. Yoshida T, Zhou XJ, Lu DH, Komiya S, Ando Y, et al. (2007) Low-energy electronic structure of the high-t_C cuprates $la_{2-x}sr_xcuo_4$ studied by angle-resolved photoemission spectroscopy. J Phys: Condens Matter 19: 125209.
119. Wen HH, Shan L, Wen XG, Wang Y, Gao H, et al. (2005) Pseudogap, superconducting energy scale, and fermi arcs of underdoped cuprate superconductors. Phys Rev B 72: 134507–1–134507–6.
120. Presland MR, Tallon JL, Buckley RG, Liu RS, Flower NE (1991) General trends in oxygen stoichiometry effects on t_C in bi and tl superconductors. Physica C 176: 95–105.
121. Ong NP, Wang Y, Ono S, Ando Y, Uchida S (2004) Vorticity and the nernst effect in cuprate superconductors. Ann Phys 13: 9–14.
122. Rullier-Albenque F, Tourbot R, Alloul H, Lejay P, Colson D, et al. (2006) Nernst effect and disorder in the normal state of high-t_C cuprates. Phys Rev Lett 96: 067002–1–067002–4.
123. Xu ZA, Shen JQ, Zhao SR, Zhang YJ, Ong CK (2005) Nernst effect and superconducting fluctuations in zn-doped $yba_2cu_3o_{7-\delta}$. Phys Rev B 72: 144527–1–144527–5.
124. Li P, Mandal S, Budhani RC, Greene RL (2007) Correlation between incoherent phase fluctuations and disorder in $y_{1-x}pr_xba_2cu_3o_{7-\delta}$ epitaxial films from nernst effect measurements. Phys Rev B 75: 184509–1–184509–5.
125. Johannsen N, Wolf T, Sologubenko AV, Lorenz T, Freimuth A, et al. (2007) Nernst effect in $ndba_2\{cu_1-_yni_y\}3o7-\delta$ (y = 00.12). Phys Rev B 76: 020512(R)-1–020512(R)-4.
126. Tohayama T, Maekawa S (2000) Angle-resolved photoemission in high t_C cuprates from theoretical viewpoints. Supercond Sci Technol 13: R17.
127. Tohayama T, Maekawa S (2003) Doping dependence of chemical potential and entropy in holeand electron-doped high-t_C cuprates. Phys Rev B 67: 092509–1–092509–3.
128. Wang Y, Li L, Naughton MJ, Gu GD, Uchida S, et al. (2005) Field-enhanced diamagnetism in the pseudogap state of the cuprate $bi_2sr_2cacu_2o_{8+\delta}$ superconductor in an intense magnetic field. Phys Rev Lett 95: 247002–1–247002–4.
129. Kim C, White PJ, Shen ZX, Tohyama T, Shibata Y, et al. (1998) Systematics of the photoemission spectral function of cuprates: Insulators and hole- and electron-doped superconductors. Phys Rev Lett 80: 4245–4248.
130. Kulic ML, Dolgov OV (2007) Angle-resolved photoemission spectra of $bi_2sr_2cacu_2o_8$ show a coulomb coupling 1 and an electron-phonon coupling of 2 − 3. Phys Rev B 76: 132511–1–132511–4.
131. Gonnelli RS, Ummarino GA, Stepanov VA (1997) Determination of the tunneling electron-phonon spectral function in high-t_C superconductors with energy dependence of the normal density of states. Physica C 275: 162–171.
132. Khlopkin MN, Panova GK, Shikov AA, Chernoplekov NA (1999) Specific heat of the electronic superconductor $pr_{1.85}ce_{0.15}cuo_4$. Phys Solid State 41: 1050–1054.
133. Balci H, Smolyaninova VN, Fournier P, Biswas A, Greene RL (2002) Magnetic-field dependence of electronic specific heat in $pr_{1.85}ce_{0.15}cuo_4$. Phys Rev B 66: 174510–1–174510–4.
134. Li P, Greene RL (2007) Normal-state nernst effect in electron-doped $pr_{2-x}ce_xcuo_{4-\delta}$: Superconducting fluctuations and two-band transport. Phys Rev B 76: 174512–1–174512–9.
135. Zimmers A, Shi L, Schmadel DC, Fisher WM, Greene RL, et al. (2007) Infrared hall effect in the electron-doped high-t_C cuprate $pr_{2-x}ce_xcuo_4$. Phys Rev B 76: 064515–1–064515–6.
136. Hackl A, Sachdev S (2009) Nernst effect in the electron-doped cuprate superconductors. Phys Rev B 79: 235124–1–235124–9.
137. Matsuda A, Sugita S, Watanabe T (1999) Temperature and doping dependence of the $bi_{2.1}sr_{1.9}cacu_2o_{8+\delta}$ pseudogap and superconducting gap. Phys Rev B 60: 1377–1381.